COWVR Project

COWVR Algorithm Theoretical Basis Document (ATBD)

Initial

Prepared by:

_____ _____

Shannon Brown, COWVR PI Date

Jet Propulsion Laboratory, California Institute of Technology

Approved By:

_____ _____

Albert Chang,
COWVR Ground Software Engineer Date

_____ _____

Sharmila Padmanabhan,
COWVR SE Date

The research was carried out at the Jet Propulsion Laboratory, California Institute of Technology, under a contract with the National Aeronautics and Space Administration (80NM0018D0004)

The cost information contained in this document is of a budgetary and planning nature and is intended for informational purposes only. It does not constitute a commitment on the part of JPL and/or Caltech.

August 20, 2016
JPL D-81977

Jet Propulsion Laboratory
California Institute of Technology

Table of Contents

1.0 Introduction

1.1. Purpose and Scope

This COWVR Algorithm Theoretical Basis Document (ATBD) describes the forward and inverse instrument models used to process the COWVR data.

1.2. Mission Description

The Air Force (AF) plans to fly the JPL-provided Compact Ocean Wind Vector Radiometer (COWVR) instrument as a proof-of-concept technology to demonstrate ocean surface vector winds (OSVW) products consistent with WindSat on-orbit performance. A successful COWVR demonstration mission could help mitigate a potential OSVW data gap for the DoD. COWVR leverages Jason 3 Advanced Microwave Radiometer (AMR) heritage designs in the development of a low-cost, rapid development, space borne sensor providing measurements of ocean surface vector winds, precipitation, and total precipitable and cloud liquid water, all of which provide important meteorological information for the DoD.

1.3. Instrument Description

The Compact Ocean Wind Vector Radiometer (COWVR) sensor is a fully polarimetric, conically imaging microwave radiometer, operating at 18.7 GHz, 23.8 GHz, and 33.9 GHz, for measuring ocean surface vector winds (OSVW). The novel COWVR design features include:

- the use of a single multi-frequency feed horn enabling a simple antenna rotating about the feed axis (as opposed to having to spin the entire radiometer system)
- internal polarimetric calibration sources which eliminate the need for an external warm load and cold sky reflector simplifying the mechanical design
- a compact MMIC receiver implementation, lowering the system mass, power and volume

Figure 1.3-1 shows the instrument block diagram and components. Subsystems are defined as follows:

- The Electronics Unit (EU) contains three sub-elements. The Power Control Unit (PCU) provides power to all secondary power from the unregulated spacecraft bus to the instrument electronics, excluding the mechanism (motor, motor controller, and position sensor). The Data Acquisition and Control (DAC) unit communicates with the spacecraft, supplies all RF control signals, and receives all RF and housekeeping data. The Housekeeping Unit (HKU) reads all engineering voltages and temperatures and supplies them to the DAC.
- The RF Subsystem consists of the feed horn, orthomode transducer (OMT), waveguides, Noise Source Combiner Assembly (NSCA), two noise sources, two receivers, and the Polarimetric Backend Unit (PBU).
- The Mechanical and Thermal Subsystem (MTS) consists of the launch restraint, thermal control system, reflector structure assembly (RSA), Spin Mechanism Assembly (SMA), and all structures to support the various instrument sub-element chassis. The SMA includes the motor, motor controller, position sensor, and mechanism power conditioning

board.

Figure 1.3-1 COWVR Instrument Block Diagram

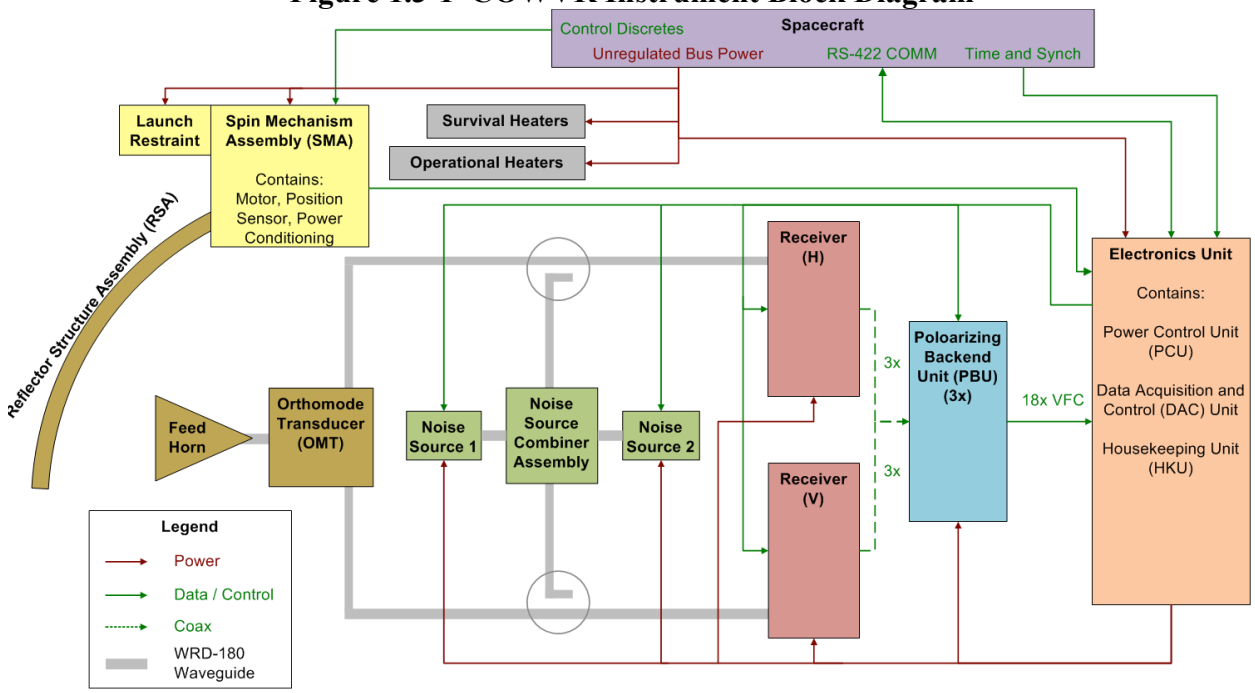

1.4. Document Structure

1.4.1. Applicable Documents

Figure 1.4-1 illustrates the COWVR requirements flow. This document is consistent and responsive to the requirements in the following requirements:

- COWVR Data Product Requirements Document (DPRD) (D-80123)

The following are consistent and responsive to this document:

- COWVR Calibration Plan

Figure 1.4-1 COWVR Requirements Flow

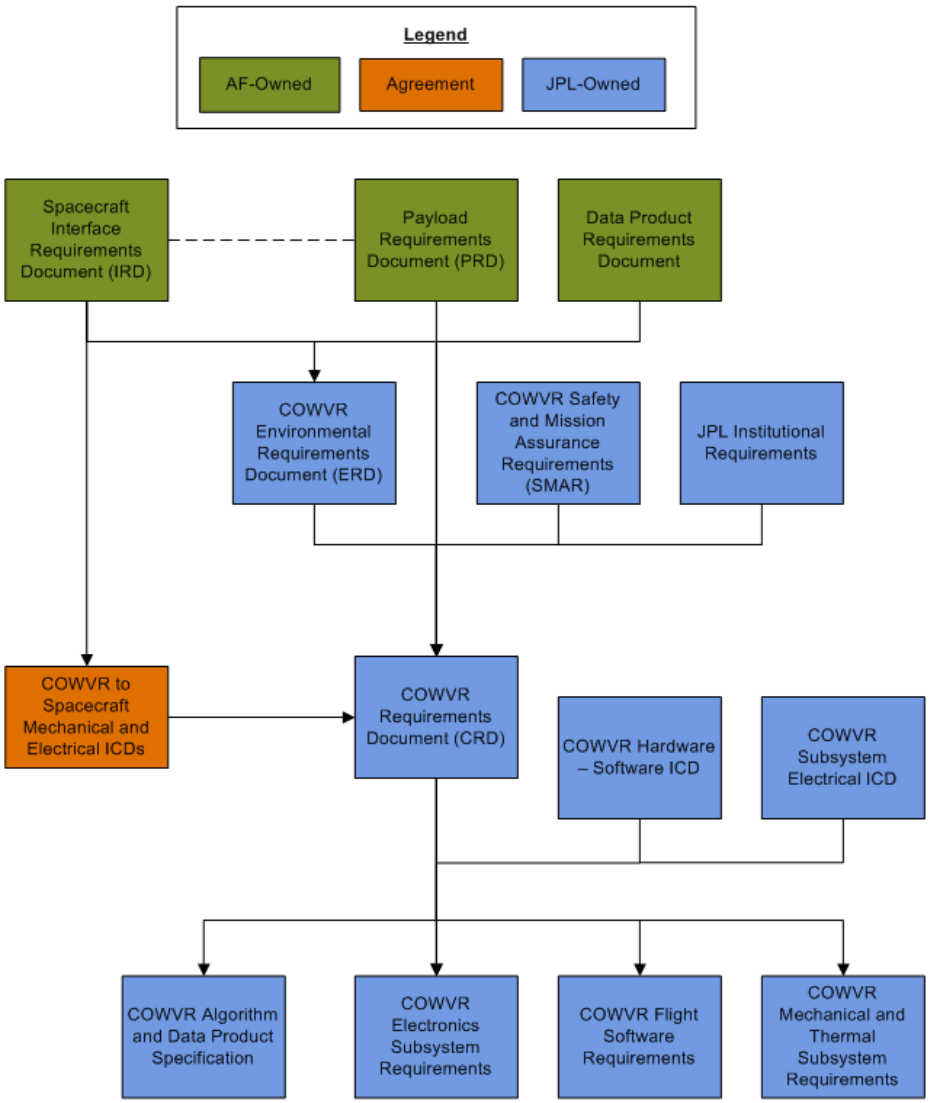

1.4.2. Acronyms

ACS	Attitude and Control System
AMR	Advanced Microwave Radiometer
ATBD	Algorithm Theoretical Basis Document
APC	Antenna Pattern Correction
CALNS	Calibration Noise Source
CFOV	Composite Field of View (weighted average of IFOV main beam measurements calculated on the ground by re-sampling algorithm)

CM	Center of Mass
CSEQ	Configuration Sequence
CSEQ	Configuration Sequence
DAC	Data Acquisition
EPBR	Electronic Polarization Basis Rotation
EPOI	Effective Product of Inertia
ES	Electronics Subsystem
II&T	Instrument Integration and Test
MSEQ	Measurement Sequence
IFOV	Instantaneous Field of View (measured main beam)
MIC	Microwave Integrated Circuit
MMIC	Monolithic Microwave Integrated Circuit
OSTM	Ocean Surface Topology Mission
OSVW	Ocean Surface Vector Winds
OMT	Ortho-mode Transducer
PBU	Polarimetric Backend Unit
PCU	Power Converter Unit
PL	Payload
PPS	Pulse Per Second
RFI	Radio Frequency Interference
RSS	Root Sum (of) Squares
SMDE	Spin Mechanism Drive Electronics
TB	Brightness Temperature
VFC	Voltage to Frequency Converter
VNA	Vector Network Analyzer

2.0 Overview of COWVR

Conically imaging passive microwave radiometer systems such as the Special Sensor Microwave Imager (SSM/I, SSMIS), the Advanced Microwave Scanning Radiometer (AMSR-E, AMSR-2) and WindSat, have been providing critical environmental data for over 30 years. But over this time, the overall sensor design has remained largely unchanged. These conical sensors have three basic attributes; (1) A large, massive spun portion containing the radiometer and electronics system; (2) A de-spun external un-polarized warm target and cold sky reflector and; (3) a large feedhorn array and individual receivers for each frequency and polarization. These design attributes drive the instrument mechanical complexity, spacecraft accommodation (e.g. momentum compensation) and instrument cost. For example, the WindSat needed to offset 189 Nms of spun momentum from the sensor (Koss and Woolaway, 2006). The sensors that were in development for NPOESS (CMIS and later MIS) were each expected to exceed 300 kg, 300 W and cost more than $100M (Chauhan, 2003). It is clear that a simplified design solution is needed to reduce the sensor mass, power, cost and accommodation, yet maintain the legacy performance.

The COWVR instrument uses an entirely different design to eliminate the instrument mechanical complexity that drives mass, power and cost. The enabling design features include (1) the use of a single multi-frequency feed horn permitting a simple antenna rotating about the feed axis, as opposed to having to spin the entire radiometer system and pass signals through the spin assembly; (2) internal calibration sources which enable fully polarimetric calibration and eliminate the need for an external warm load and cold sky reflector simplifying the mechanical design and enabling a complete 360^{o} scan and; (3) a compact highly integrated MMIC polarimetric combining receiver implementation, lowering the system mass and power which in turn makes the system well suited for deployment on smaller class, lower cost satellites.

An illustration of the COWVR instrument design is shown in Figure 2-1. The instrument includes a single stationary multi-frequency feed horn that illuminates rotating reflector generating a 360^{o} un-blocked conical scan. The reflector rotates at 30 RPM and provides a spatial resolution <35km and a swath width of 1012 km from the mission orbit altitude of 450km. After the feed, an orthomode transducer is used to separate the signal into two linear orthogonal components which are then fed via waveguide into MMIC multi-frequency receivers to amplify and filter the signals. The output from the receivers is input to a hybrid combining polarimetric backend unit which performs the analog in-phase and quadrature phase cross-correlation of the two signals to produce the +45, -45 and left and right circular polarized outputs.

The instrument is calibrated using PIN-diode switches internal to the receivers and a correlated noise source. The switches are used to toggle each receiver between an ambient reference load and the antenna. The correlated noise source is capable of generating known polarized signals by injecting correlated noise with a defined phase offset between the two receiver chains.

Because the feedhorn is fixed, the instrument polarization is fixed to the instrument frame and rotates relative to the Earth polarization basis. Because the instrument measures the full stokes vector, which completely describes the polarization state of the scene, a simple geometric

transform is used in ground processing to rotate the polarization from the fixed instrument frame to the Earth frame. This technique has been previously used in groundbased and airborne radiometer systems and is commonly referred to as Electronic Polarization Basis Rotation (EPBR) (Gasiewski et al., 1992; Lahtinen et al,. 2003). This actually presents a calibration advantage which is discussed further in the COWVR calibration plan.

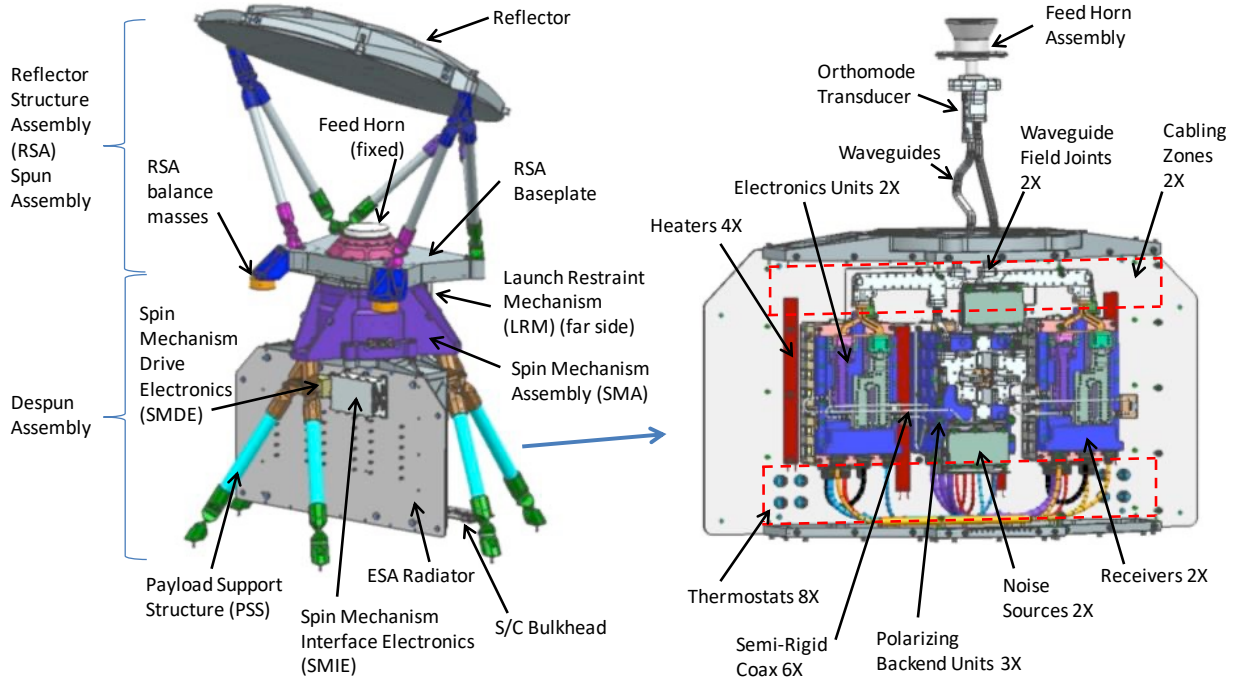

Figure 2-1. CAD representation of the COWVR instrument.

3.0 COWVR Processing Overview

The following flow charts represent the high-level processing flow from raw COWVR telemetry to wind vector and other geophysical retrieval products. These algorithms are described in the following sections.

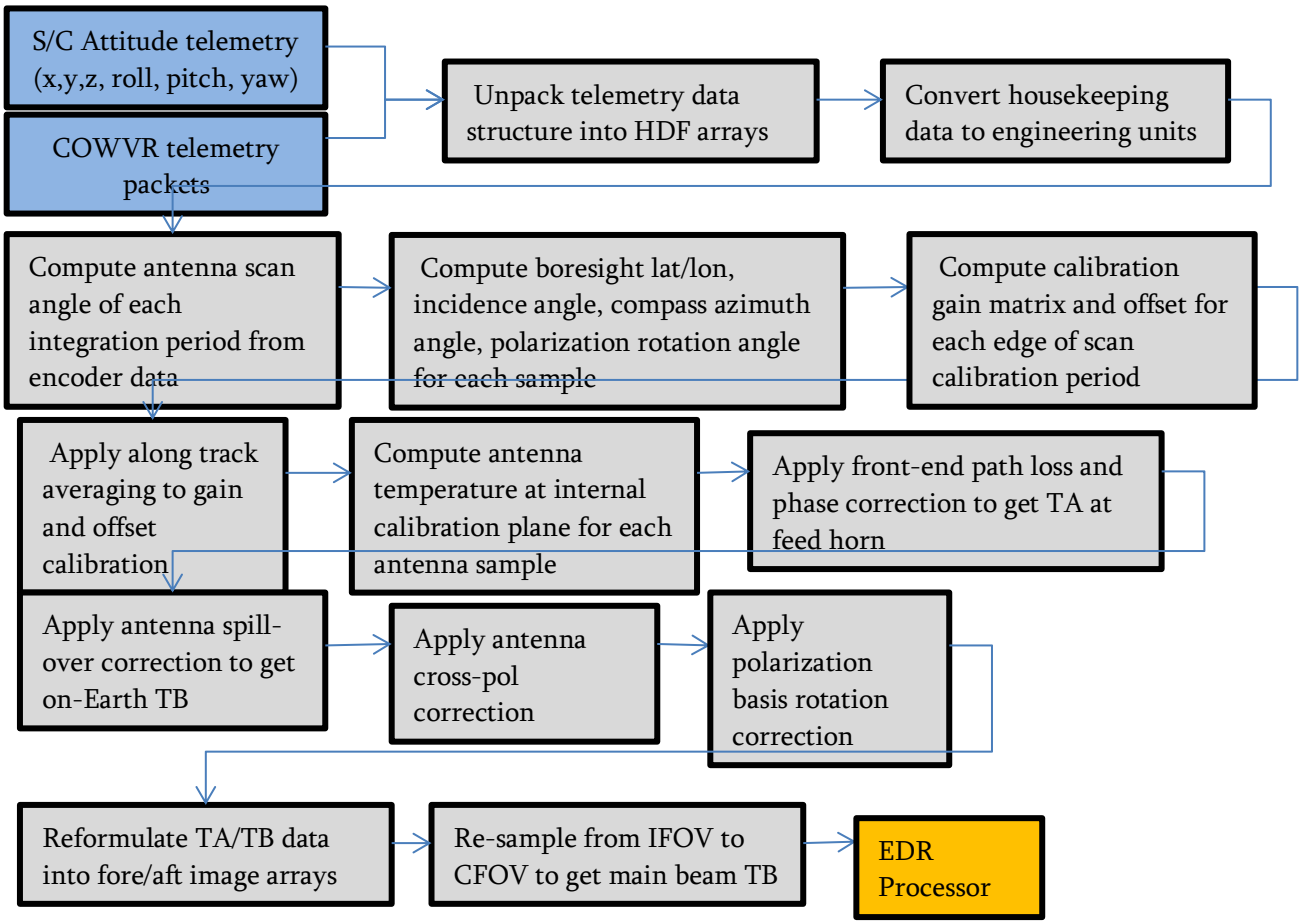

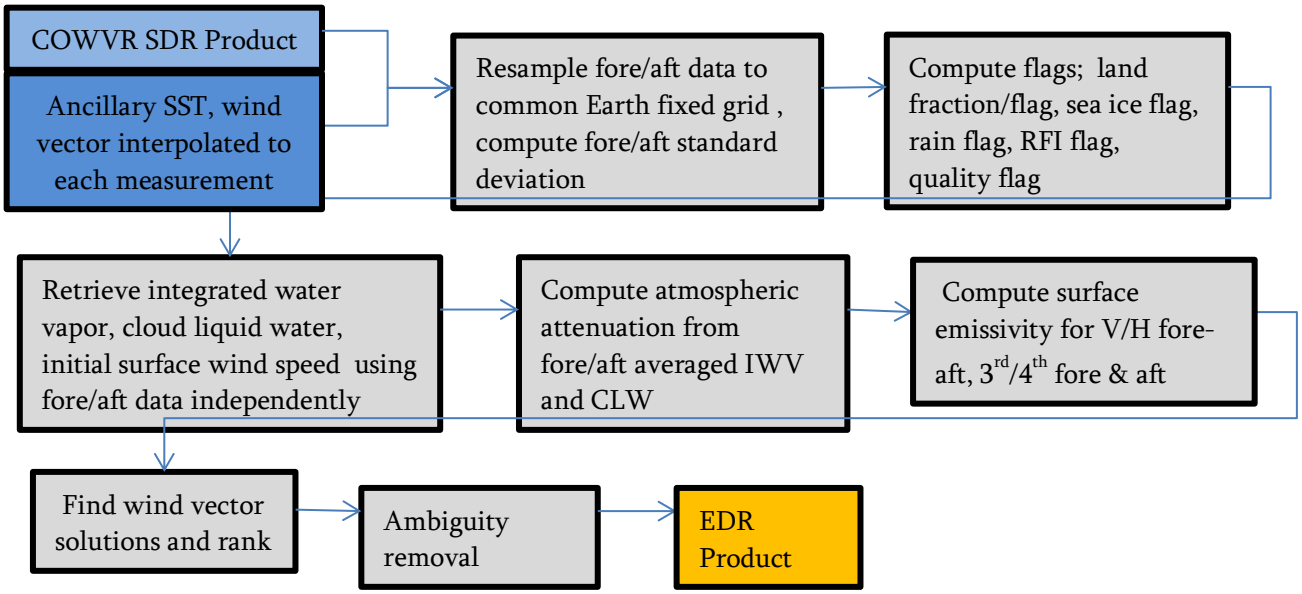
COWVR SDR Product
Ancillary SST, wind vector interpolated to each measurement
Resample fore/aft data to common Earth fixed grid , compute fore/aft standard deviation
Compute flags; land fraction/flag, sea ice flag, rain flag, RFI flag, quality flag
Retrieve integrated water vapor, cloud liquid water, initial surface wind speed using fore/aft data independently
Compute atmospheric attenuation from fore/aft averaged IWV and CLW
Compute surface emissivity for V/H fore-aft, 3rd/4th fore & aft
Find wind vector solutions and rank
Ambiguity removal
EDR Product

4.0 COWVR Calibration Algorithms

4.1. Forward Model

The COWVR instrument forward model describes the signal propagation through the COWVR instrument. It is most insightful to begin with the radiation incident on the COWVR antenna aperture. In the equations below, the double bars indicate a matrix and the single bars indicate a vector.

The brightness temperature incident on the COWVR antenna aperture at frequency f and from direction (θ,ϕ) can be represented by the modified Stokes vector,

$$\overline{T}_B = \begin{bmatrix} T_V \\ T_H \\ T_3 \\ T_4 \end{bmatrix} = \begin{bmatrix} T_V \\ T_H \\ T_{+45} - T_{-45} \\ T_{LCP} - T_{RCP} \end{bmatrix} = \frac{\lambda^2}{\eta k B} \begin{bmatrix} \left|E_V\right|^2 \\ \left|E_H\right|^2 \\ 2\,\mathrm{Re}\left|E_V E_H^*\right| \\ 2\,\mathrm{Im}\left|E_V E_H^*\right| \end{bmatrix} \tag{3.1}$$

where the vertical and horizontal polarizations are relative to the Earth normal

$$\hat{h} = \frac{\hat{k} \times \hat{n}}{\left|\hat{k} \times \hat{n}\right|} \tag{3.2a}$$

$$\hat{v} = \hat{h} \times \hat{k} \tag{3.2b}$$

where k is a vector pointing along the instrument boresight look direction.

The instrument polarization is fixed and rotated relative to the Earth polarization by an angle α. The angle depends on the orientation of the feed horn, instrument and spacecraft. The angle is also a function of look angle away from boresight. A rotation matrix is used to transform the polarization from the Earth basis to the antenna basis,

$$\overline{\overline{R}}(\alpha) = \begin{bmatrix} \cos^2\alpha & \sin^2\alpha & \frac{1}{2}\sin 2\alpha & 0 \\ \sin^2\alpha & \cos^2\alpha & -\frac{1}{2}\sin 2\alpha & 0 \\ -\sin 2\alpha & \sin 2\alpha & \cos 2\alpha & 0 \\ 0 & 0 & 0 & 1 \end{bmatrix} \tag{3.3}$$

Thus, the apparent brightness temperature at the aperture of the antenna is

$$\overline{T}_{BI}(f,\theta,\phi) = \overline{\overline{R}}(\alpha)\overline{T}_B(f,\theta,\phi) \tag{3.4}$$

The antenna system collects the energy over a sphere weighted by the antenna pattern. A formulation for the Stokes antenna pattern is given by [1] and is expressed as,

$$\overline{T}_A(f) = \int_{4\pi} \overline{\overline{F}}(f,\theta,\phi)\overline{T}_{BI}(f,\theta,\phi)d\Omega \tag{3.5}$$

where the *F* matrix is formed from the complex co-pol and cross-pol antenna patterns

$$\overline{\overline{F}}(f,\theta,\phi) = \begin{bmatrix} |f_{VV}|^2 & |f_{VH}|^2 & \mathrm{Re}\, f_{VV} f_{VH}^* & -\mathrm{Im}\, f_{VV} f_{VH}^* \\ |f_{HV}|^2 & |f_{HH}|^2 & \mathrm{Im}\, f_{HH} f_{HV}^* & \mathrm{Re}\, f_{HH} f_{HV}^* \\ 2\,\mathrm{Re}\, f_{VV} f_{HV}^* & 2\,\mathrm{Re}\, f_{HH} f_{VH}^* & \mathrm{Re}\, f_{VV} f_{HH}^* + \mathrm{Re}\, f_{VH} f_{HV}^* & \mathrm{Im}\, f_{VH} f_{HV}^* - \mathrm{Im}\, f_{VV} f_{HH}^* \\ 2\,\mathrm{Im}\, f_{VV} f_{HV}^* & -2\,\mathrm{Im}\, f_{HH} f_{VH}^* & \mathrm{Im}\, f_{VV} f_{HH}^* + \mathrm{Im}\, f_{VH} f_{HV}^* & \mathrm{Re}\, f_{VV} f_{HH}^* - \mathrm{Re}\, f_{VH} f_{HV}^* \end{bmatrix}$$

and the terms in the matrix are functions of (f,θ,ϕ).

The antenna temperature in equation 3.5 is input to the COWVR orthomode transducer (OMT). This elliptically polarized signal is decomposed into two orthogonal linear components by the OMT, amplified and filtered by two independent receivers and fed into a polarimetric back end unit which detects the total power of each linear component and the total power of the in-phase and quadrature phase cross correlation of the two linearly polarized signals. The outputs of the 6-ports of the polarimetric backend are illustrated mathematically in Figure 3-1.

The instrument front end (the components from the feed horn to the input of the receiver) acts to attenuate the signals and add a phase offset between two linear components. The effect of the phase offset is to mix T3 into T4. The effect of the front end loss is to introduce a signal proportional to the temperature of the front end components and reduce the end-to-end system gain.

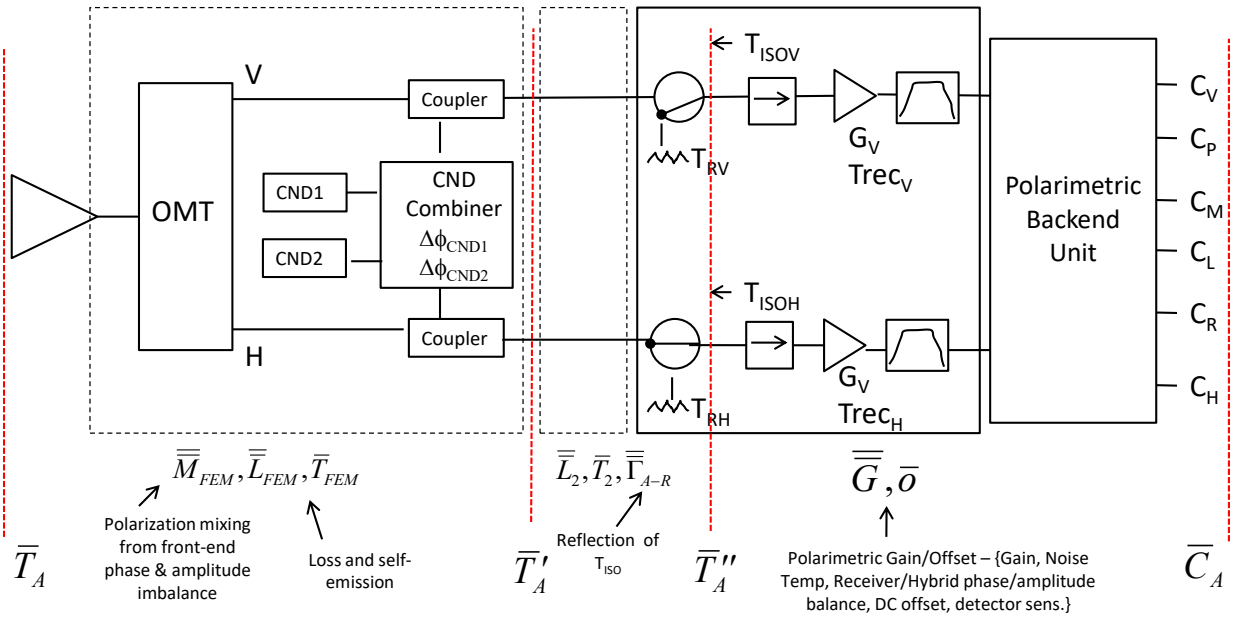

Figure 3-1. COWVR antenna temperature calibration forward model.

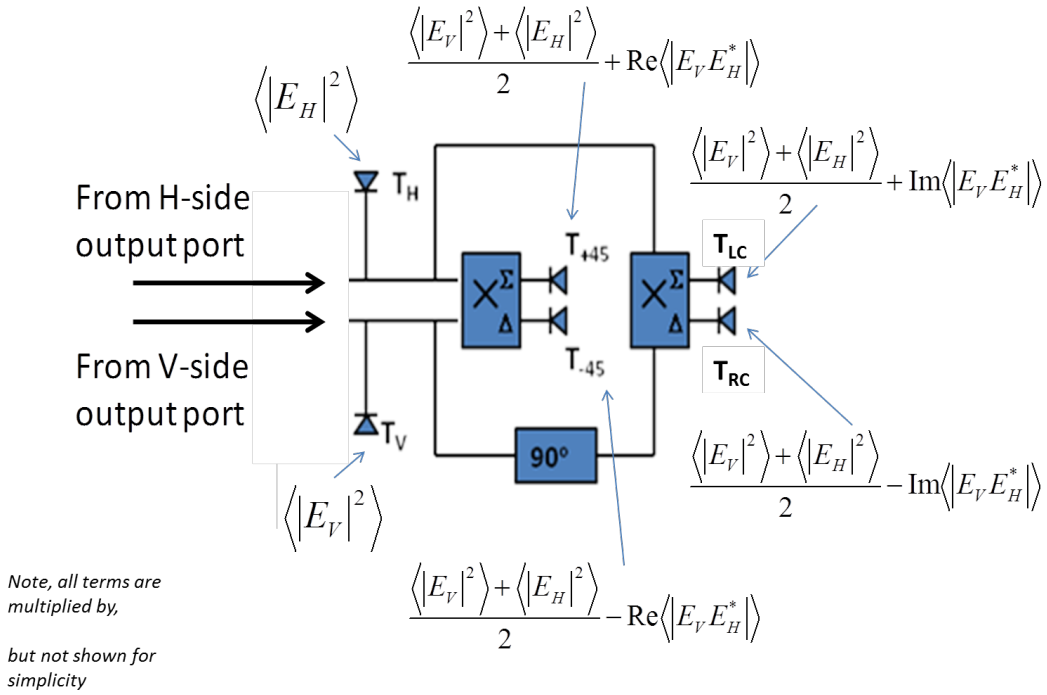

Figure 3-2. Mathematical representation of each output port of the PBU.

The primed antenna temperature at the first plane shown in Figure 3-1 is given by

$$\overline{T}_A' = \left(\overline{\overline{I}} - \overline{\overline{L}}_{FEM}\right)\overline{\overline{M}}_{FEM}\overline{T}_A + \overline{\overline{L}}_{FEM}\overline{T}_{FEM} \tag{3.6}$$

where M is the Mueller matrix of the front end manifold, L is the loss matrix of the front end and T is the physical temperature vector of the front end. The double bars indicate a matrix and the single bars indicate a vector. The Mueller matrix accounts for the mixing between polarizations due to phase and amplitude offsets in the front end.

The Mueller matrix of the OMT is represented by [1]

$$M_{OMT} = \begin{bmatrix} |S_{VV}|^2 & |S_{VH}|^2 & \mathrm{Re}\,S_{VV}S_{VH}^* & -\mathrm{Im}\,S_{VV}S_{VH}^* \\ |S_{HV}|^2 & |S_{HH}|^2 & \mathrm{Im}\,S_{HH}S_{HV}^* & \mathrm{Re}\,S_{HH}S_{HV}^* \\ 2\,\mathrm{Re}\,S_{VV}S_{HV}^* & 2\,\mathrm{Re}\,S_{HH}S_{VH}^* & \mathrm{Re}\,S_{VV}S_{HH}^* + \mathrm{Re}\,S_{VH}S_{HV}^* & \mathrm{Im}\,S_{VH}S_{HV}^* - \mathrm{Im}\,S_{VV}S_{HH}^* \\ 2\,\mathrm{Im}\,S_{VV}S_{HV}^* & -2\,\mathrm{Im}\,S_{HH}S_{VH}^* & \mathrm{Im}\,S_{VV}S_{HH}^* + \mathrm{Im}\,S_{VH}S_{HV}^* & \mathrm{Re}\,S_{VV}S_{HH}^* - \mathrm{Re}\,S_{VH}S_{HV}^* \end{bmatrix} \tag{3.7}$$

In the case of good port-to-port isolation, as is in the case of COWVR (> 50dB), this matrix is approximated by,

$$M_{OMT} = \begin{bmatrix} |S_{VV}|^2 & 0 & 0 & 0 \\ 0 & |S_{HH}|^2 & 0 & 0 \\ 0 & 0 & |S_{VV}||S_{HH}| & 0 \\ 0 & 0 & 0 & |S_{VV}||S_{HH}| \end{bmatrix} \begin{bmatrix} 1 & 0 & 0 & 0 \\ 0 & 1 & 0 & 0 \\ 0 & 0 & \cos(\Delta\theta) & \sin(\Delta\theta) \\ 0 & 0 & -\sin(\Delta\theta) & \cos(\Delta\theta) \end{bmatrix} \tag{3.8}$$

which gives insight into the front end effect on the signal. The matrix on the left accounts for the path loss (ohmic and reactive losses) and the matrix on the right accounts for the rotation between the 3rd and 4th stokes channels due to a H/V phase imbalance ($\Delta\theta = \theta_V - \theta_H$).

Care must be taken to define a phase reference plane between the antenna and the RF front end to ensure phase differences are not accounted for twice. For COWVR, it is natural to enforce phase balance in the antenna patterns and apply all phase offsets as a part of the antenna temperature calibration process. This is because the antenna patterns are expected to be referenced to the feed horn output.

An effective reflection plane is placed just after the front end manifold (FEM), so the path loss assumed in the FEM is from ohmic loss. The loss matrix is given by

$$L_{FEM} = \begin{bmatrix} L_V & 0 & 0 & 0 \\ 0 & L_H & 0 & 0 \\ 0 & 0 & \sqrt{L_V L_H} & 0 \\ 0 & 0 & 0 & \sqrt{L_V L_H} \end{bmatrix} \tag{3.9}$$

and the physical temperature vector is given by

$$\overline{T}_{FEM} = \begin{bmatrix} T_{FEM\_V} \\ T_{FEM\_H} \\ 0 \\ 0 \end{bmatrix}. \tag{3.10}$$

Note, the self emission from the front end is uncorrelated between H and V and does not impact the 3rd and 4th Stokes antenna temperatures. To the extent of ideal port-to-port isolation, the only impact of the front end on the 3rd and 4th Stokes channels is to attenuate the signal and rotate (mix) the signal between 3rd and 4th Stokes.

The double primed antenna temperature at the second calibration plane in 3-1 is given by

$$\overline{\overline{T}}_A'' = \left(\overline{\overline{I}} - \overline{\overline{\Gamma}}_{A-R}\right)\left(\left(\overline{\overline{I}} - \overline{\overline{L}}_2\right)\overline{\overline{T}}_A' + \overline{\overline{L}}_2\overline{\overline{T}}_2\right) + \overline{\overline{\Gamma}}_{A-R}\overline{\overline{T}}_{iso} \tag{3.11}$$

where $\Gamma_{A\text{-}R}$ is an effective coherent reflection coefficient matrix looking from the receiver into the feed horn, L_2 is the loss of the coupler and T_2 its temperature and T_{iso} is the temperature of the isolator in the receiver. The loss matrix and temperature vector are represented equivalently as

in equations 3.9 and 3.10 and the reflection coefficient matrix is equivalent in form to equation 3.9.

The vector of 6 counts at the output of the PBU is given by

$$\overline{C}_A = \overline{\overline{G}}\,\overline{T}_A'' + \overline{o} \tag{3.12}$$

where *G* is the polarimetric gain of the radiometer and *o* is the polarimetric offset [2]. Equation 3.12 expands to

$$\begin{bmatrix} C_{V,AA} \\ C_{H,AA} \\ C_{p,AA} \\ C_{m,AA} \\ C_{L,AA} \\ C_{R,AA} \end{bmatrix} = \begin{bmatrix} G_{VV} & G_{VH} & G_{V3} & G_{V4} \\ G_{HV} & G_{HH} & G_{H3} & G_{H4} \\ G_{pV} & G_{pH} & G_{p3} & G_{p4} \\ G_{mV} & G_{mH} & G_{m3} & G_{m4} \\ G_{LV} & G_{LH} & G_{L3} & G_{L4} \\ G_{RV} & G_{RH} & G_{R3} & G_{R4} \end{bmatrix} \begin{bmatrix} T''_V \\ T''_H \\ T''_3 \\ T''_4 \end{bmatrix} + \begin{bmatrix} o_V \\ o_H \\ o_p \\ o_m \\ o_L \\ o_R \end{bmatrix} \tag{3.13}$$

4.2. Antenna Temperature Calibration

To determine the antenna temperature at the input (eqn 3.5), each term in equations 3.7 – 3.12 must be known. Because the polarimetric gain and offset of the receivers is highly variable in time, stable internal calibration sources are included in the design. These calibration sources consist of a correlated noise source that is capable of injecting known polarized signals into the polarimeter and PIN-diode Dicke switches which independently toggle each receiver between the antenna and an ambient termination. The correlated noise source consists of two noise source units which are combined via a hybrid combining network and coupled into each receiver chain via waveguide couplers. The hybrid combining network couples one noise source with approximately equal phase into each receiver. A roughly 90-degree phase shift is added to one leg of the combining network to introduce a phase difference between the receivers. Together, these sources provide enough information to estimate the full polarimetric gain and offset of the receiver. The 3rd and 4th stokes signals injected by the noise source is dependent on the relative phase of the noise diode brightness between the H and V chains and is given by

$$
\begin{aligned}
T_{ND1,3} &= 2\cos(\Delta\phi_1)\sqrt{T_{ND1,V}T_{ND1,H}} \\
T_{ND1,4} &= 2\sin(\Delta\phi_1)\sqrt{T_{ND1,V}T_{ND1,H}} \\
T_{ND2,3} &= 2\cos(\Delta\phi_2)\sqrt{T_{ND2,V}T_{ND2,H}} \\
T_{ND2,4} &= 2\sin(\Delta\phi_2)\sqrt{T_{ND2,V}T_{ND2,H}}
\end{aligned}
\tag{3.14}
$$

The V/H phase differences between the two noise diodes must be sufficiently different and not equal to 180 degrees. A relative phase difference of 90 degrees is best $(\Delta\varphi_2 - \Delta\varphi_1) = 90^0$. For COWVR, the phase shift is roughly 70 – 80 degrees.

The polarimetric gain and offset in eqn. 3.12 are estimated by exercising the various possible calibration states. Note, V and H here refer to the instrument polarization basis and do not necessarily line up with the Earth V and H polarizations. The possible calibration states are shown in Figure 3-3:

	V	H	Counts Pneumonic β=V,H,P,M,L,R
Scene	Antenna	Antenna	$C_{\beta,AA}$
Calibration	Reference	Reference	$C_{\beta,RR}$
	Antenna + CND1	Antenna + CND1	$C_{\beta,ND1+AA}$
	Reference	Antenna + CND1	$C_{\beta,ND1+RA}$
	Antenna + CND1	Reference	$C_{\beta,ND1+AR}$
	Antenna + CND2	Antenna + CND2	$C_{\beta,ND2+AA}$
	Reference	Antenna + CND2	$C_{\beta,ND2+RA}$
	Antenna + CND2	Reference	$C_{\beta,ND2+AR}$
	Reference	Antenna	$C_{\beta,RA}$
	Antenna	Reference	$C_{\beta,AR}$

Figure 3-3. COWVR internal calibration states and pneumonics.

4.2.1. Case of Ideal Switch Isolation

The calibration equations are first developed for the case of ideal switch isolation (e.g. no leakage between antenna/reference ports), which provides a simplified conceptual overview of how each calibration state contributes the estimate of the gain matrix and offset vector. The next section develops the equations for good, but finite switch isolation, which is the reality for COWVR. For perfect switch isolation, the calibration states are represented by the following equations, assuming the receiver chains are sufficiently isolated. These equations also assume that there are no state dependent offsets in the measurements. In the following β=P or M for 3rd stokes and β=L or R for 4th stokes. Note, the overbar and double-prime of the antenna temperature were suppressed for clarity.

$$C_{\beta,AA} = G_{\beta,V}T_{A,V} + G_{\beta,H}T_{A,H} + G_{\beta,3}T_{A,3} + G_{\beta,4}T_{A,4} + o_\beta \quad (3.15a)$$

$$C_{\beta,RR} = G_{\beta,V}T_{R,V} + G_{\beta,H}T_{R,H} + o_\beta \quad (3.15b)$$

$$C_{\beta,ND1+AA} = G_{\beta,V}\left(T_{ND1,V} + T_{A,V}\right) + G_{\beta,H}\left(T_{ND1,H} + T_{A,H}\right) + G_{\beta,3}\left(T_{ND1,3} + T_{A,3}\right) + G_{\beta,4}\left(T_{ND1,4} + T_{A,4}\right) + o_\beta \quad (3.15c)$$

$$C_{\beta,ND2+AA} = G_{\beta,V}\left(T_{ND2,V} + T_{A,V}\right) + G_{\beta,H}\left(T_{ND2,H} + T_{A,H}\right) + G_{\beta,3}\left(T_{ND2,3} + T_{A,3}\right) + G_{\beta,4}\left(T_{ND2,4} + T_{A,4}\right) + o_\beta \quad (3.15d)$$

$$C_{\beta,ND1+AR} = G_{\beta,V}\left(T_{ND1,V} + T_{A,V}\right) + G_{\beta,H}T_{R,H} + o_\beta \quad (3.15e)$$

$$C_{\beta,ND1+RA} = G_{\beta,V}T_{R,V} + G_{\beta,H}\left(T_{ND1,H} + T_{A,H}\right) + o_\beta \quad (3.15f)$$

$$C_{\beta,AR} = G_{\beta,V}T_{A,V} + G_{\beta,H}T_{R,H} + o_\beta \quad (3.15g)$$

$$C_{\beta,RA} = G_{\beta,V}T_{R,V} + G_{\beta,H}T_{A,H} + o_\beta \quad (3.15h)$$

The calibration states in 3.15 form an over-determined set of equations with which to solve for the radiometer gain matrix and offset vector at the internal calibration plane. An illustration of the 5 steps needed to estimate each parameter in eqn 3.15 is shown in Figure 3-4 below

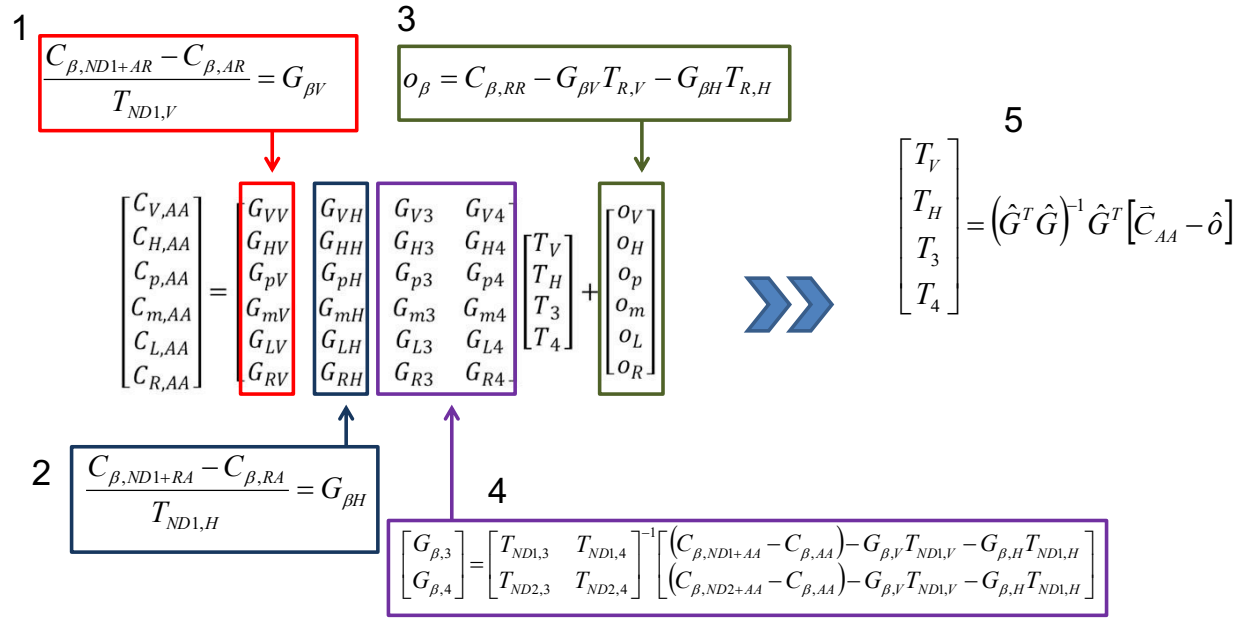

Figure 3-4. Steps to solve for the antenna temperature at the internal calibration plane.

The antenna temperature vector represented in Figure 3-4 is the equivalent antenna temperature

at the internal calibration plane. To obtain the antenna temperature at the input to the feed, which is the desired quantity, one must invert eqn. 3.6 and 3.11 to obtain,

$$\overline{T}_A = A^{-1}\left[\overline{T}_A'' - \left(\overline{\overline{I}} - \overline{\overline{\Gamma}}_{A-R}\right)\left(\overline{\overline{I}} - \overline{\overline{L}}_2\right)\overline{\overline{L}}_{FEM}\overline{T}_{FEM} - \left(\overline{\overline{I}} - \overline{\overline{\Gamma}}_{A-R}\right)\overline{\overline{L}}_2\overline{T}_2 - \overline{\overline{\Gamma}}_{A-R}\overline{T}_{iso}\right]$$
$$A = \left(\overline{\overline{I}} - \overline{\overline{\Gamma}}_{A-R}\right)\left(\overline{\overline{I}} - \overline{\overline{L}}_2\right)\left(\overline{\overline{I}} - \overline{\overline{L}}_{FEM}\right)M_{FEM} \tag{3.16}$$

The right hand side of eqn. 3.16 is the COWVR calibrated antenna temperature vector.

4.2.2. Antenna Temperature Calibration – Finite Switch Isolation

The PIN-diode switch isolation for COWVR is about 35dB for an incoherent signal, which is adequate for a non-polarimetric radiometer. However, the isolation for the coherent signal from the CND can be half of this depending on the phase of the leaked signal. The PIN-diode switches are used to estimate the individual receiver gains of the V/H-pol channels using the noise diodes turned on in the A/R and R/A states above. In the case of ideal switch isolation, only the channel with the switch looking at the antenna port would see the signal from the noise diode, the other channel would see the reference load and there would be no polarimetric signal. But since the isolation could be as low as 17dB for a coherent signal (depending on the phase through the isolated path), the noise diode in the A/R and R/A state will produce a small signal in the 3rd/4th polarimetric channels. This is accounted for in the following equations.

Gain and Offset Calibration

The polarimetric gain matrix and the offset vector can be estimated row-by-row from :

$$\bar{x}_\beta = \left(\overline{\overline{T}}_{CAL}^T\overline{\overline{T}}_{CAL}\right)\overline{\overline{T}}_{CAL}^T\overline{C}_\beta = \left[G_{\beta V} \quad G_{\beta H} \quad G_{\beta 3} \quad G_{\beta 4} \quad o_\beta\right]^T \tag{3.17}$$

for

$$\beta = V, H, P, M, L, R$$

where

$$\overline{C}_\beta = \begin{bmatrix} C_{\beta,ND1+AA} - C_{\beta,AA} \\ C_{\beta,ND2+AA} - C_{\beta,AA} \\ C_{\beta,ND1+RA} - C_{\beta,RA} \\ C_{\beta,ND1+AR} - C_{\beta,AR} \\ C_{\beta,RR} \end{bmatrix} \tag{3.18}$$

$$\overline{\overline{T}}_{CAL} = \begin{bmatrix} T_{ND1V} & T_{ND1H} & T_{ND13} & T_{ND14} & 0 \\ T_{ND2V} & T_{ND2H} & T_{ND23} & T_{ND24} & 0 \\ T_{RAV} & T_{RAH} & T_{RA3} & T_{RA4} & 0 \\ T_{ARV} & T_{ARH} & T_{AR3} & T_{AR4} & 0 \\ T_{RV} & T_{RH} & 0 & 0 & 1 \end{bmatrix} \tag{3.19}$$

and

$$\overline{T}_{RA} = \begin{bmatrix} |\alpha_V|^2 & 0 & 0 & 0 \\ 0 & 1 & 0 & 0 \\ 0 & 0 & |\alpha_V| & 0 \\ 0 & 0 & 0 & |\alpha_V| \end{bmatrix} \begin{bmatrix} 1 & 0 & 0 & 0 \\ 0 & 1 & 0 & 0 \\ 0 & 0 & \cos(\Delta\varphi_{\alpha V}) & \sin(\Delta\varphi_{\alpha V}) \\ 0 & 0 & -\sin(\Delta\varphi_{\alpha V}) & \cos(\Delta\varphi_{\alpha V}) \end{bmatrix} \begin{bmatrix} T_{ND1V} \\ T_{ND1H} \\ T_{ND13} \\ T_{ND14} \end{bmatrix} \tag{3.20a}$$

$$\overline{T}_{AR} = \begin{bmatrix} 1 & 0 & 0 & 0 \\ 0 & |\alpha_H|^2 & 0 & 0 \\ 0 & 0 & |\alpha_H| & 0 \\ 0 & 0 & 0 & |\alpha_H| \end{bmatrix} \begin{bmatrix} 1 & 0 & 0 & 0 \\ 0 & 1 & 0 & 0 \\ 0 & 0 & \cos(\Delta\varphi_{\alpha H}) & \sin(\Delta\varphi_{\alpha H}) \\ 0 & 0 & -\sin(\Delta\varphi_{\alpha H}) & \cos(\Delta\varphi_{\alpha H}) \end{bmatrix} \begin{bmatrix} T_{ND1V} \\ T_{ND1H} \\ T_{ND13} \\ T_{ND14} \end{bmatrix} \tag{3.20b}$$

and

T_{RV}, T_{RH} is the reference load (receiver) temperature either the V or H channel and either the 18/23 or 34 GHz thermistor.

The noise diode brightness varies as a function of temperature which is parameterized as a third-order polynominal. In 3.21, the equation is referenced to 300K to give more meaning to the offset coefficient.

$$T_{NDx,\beta} = a_{0\_x,\beta} + a_{1\_x,\beta}\left(TNS_x - 300\right) + a_{2\_x,\beta}\left(TNS_x - 300\right)^2 + a_{3\_x,\beta}\left(TNS_x - 300\right)^3 \tag{3.21}$$

where x = 1 or 2 and $\beta = V, H$ and TNS_x is the noise source unit thermistor temperature for x = 1 or 2

The 3rd and 4th stokes brightness for the noise source is given by

$$\begin{aligned} T_{ND1,3} &= 2\cos(\Delta\phi_{NSCA1})\sqrt{T_{ND1,V}T_{ND1,H}} \\ T_{ND1,4} &= 2\sin(\Delta\phi_{NSCA1})\sqrt{T_{ND1,V}T_{ND1,H}} \\ T_{ND2,3} &= 2\cos(\Delta\phi_{NSCA2})\sqrt{T_{ND2,V}T_{ND2,H}} \\ T_{ND2,4} &= 2\sin(\Delta\phi_{NSCA2})\sqrt{T_{ND2,V}T_{ND2,H}} \end{aligned} \tag{3.22}$$

Description of Operational Calibration Modes

During nominal operations, COWVR is configured in a so called position triggered calibration mode. In this mode, the radiometer is set to the Ant/Ant state to make measurements of the scene over the scan until it is triggered into a calibration mode at +/- 25° scan edge, as illustrated in Figure 3.2-1.

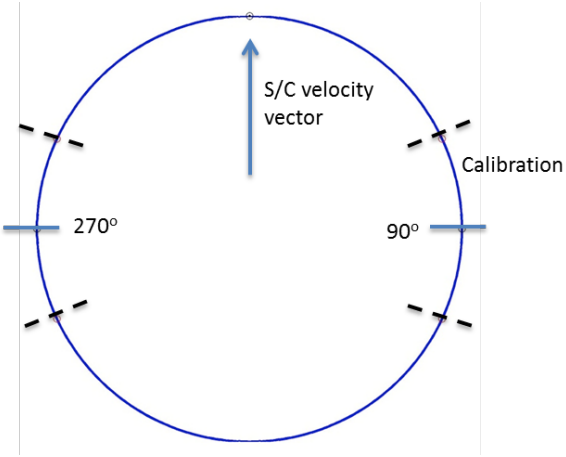

Figure 3.2-1. Illustration of the COWVR calibration mode relative to the scan

Once triggered, it begins executing up to three additional 20-measurement length (0.1s) sequences, each N times. N can be set to 0 if less than three sequences are needed. The COWVR flight software uses a look-up table of 15 sequences, each 20 measurements long to configure the state for each integration period. Grouped sequences are constructed to be able to select between calibrating 0x, 1x, 2x, 3x or 4x per edge of scan calibration period (~ once per second). After the calibration sequences complete, the software returns to the nominal Ant,Ant scene sequence until the next trigger at the other scan edge.

The calibration sequences include the following 13 element group of instrument states which provides all the states needed to construct the calibration counts vector in eqn 3.18 and solve for the gain matrix and offset vector using eqn 3.17. The gain and offset computed from this group are considered valid at the center time of the group.

C_{AR}, C_{ND1+AR}, C_{AR} ,
C_{AA}, C_{ND2+AA}, C_{AA} ,
C_{RA}, C_{ND1+RA}, C_{RA} ,
C_{AA}, C_{ND1+AA}, C_{AA} ,
C_{RR}

In position triggered mode, depending on the configuration rows used, this group will be executed 1, 2, 3 or 4 times in a row after receipt of the calibration encoder pulse, providing up to 4 independent estimates of the gain and offset during each calibration period (roughly once per second). The nominal case for COWVR is to calibrate 3x per calibration window, meaning this group will be executed 3 times and there will be three independent estimates of the gain matrix and offset vector at each edge of scan. Note, for states where a noise diode is fired, the

equivalent state with the noise diode off is executed immediately before and after the on state and the two "ND off" measurements are averaged when computing the differences in eqn 3.18. This improves performance when the scene is varying significantly over a 5ms integration period (e.g. land crossing). Defining the 13 measurements in the sequence s_1-s_{13}, this can be represented as

$$\overline{C}_\beta(\bar{s}) = \begin{bmatrix} C_{\beta,ND1+AA}(s_2) - 0.5\left(C_{\beta,AA}(s_1) + C_{\beta,AA}(s_3)\right) \\ C_{\beta,ND2+AA}(s_5) - 0.5\left(C_{\beta,AA}(s_4) + C_{\beta,AA}(s_6)\right) \\ C_{\beta,ND1+RA}(s_8) - 0.5\left(C_{\beta,RA}(s_7) + C_{\beta,RA}(s_9)\right) \\ C_{\beta,ND1+AR}(s_{11}) - 0.5\left(C_{\beta,AR}(s_9) + C_{\beta,AR}(s_{12})\right) \\ C_{\beta,RR}(s_{13}) \end{bmatrix} \tag{3.23}$$

Calibration Averaging

Because the gain and offset matrix are constructed from noisy measurements, averaging of several measurements in time is required. First, the gain/offset measurements from one edge of scan calibration period (up to 4) are averaged forming a time series of calibration measurements sampled at roughly 1Hz at each edge of scan. These 1Hz samples are then averaged using a Gaussian low-pass filter, which is represented in the time domain as,

$$\overline{G}_{i,j}(t) = \frac{\sum_{\tau=t-\Delta t_{CAL}}^{\tau=t+\Delta t_{CAL}} w(\tau) G_{i,j}(\tau)}{\sum_{\tau=t-\Delta t_{CAL}}^{\tau=t+\Delta t_{CAL}} w(\tau)} \tag{3.24a}$$

for each element i,j of the gain matrix where Δt_{CAL} is the length of the calibration running average window and

$$w(\tau) = \left(\frac{1}{\sigma_{CAL}\sqrt{2\pi}}\right)\exp\left(-\frac{(t-\tau)^2}{2\sigma^2{}_{CAL}}\right) \tag{3.24b}$$

where σ_{CAL} defines the width of the Gaussian filter. The offset is averaged in the same way using eqn 3.24.

The result is a low-pass filtered time series of 1Hz calibration measurements. These measurements are linearly interpolated in time to each Ant/Ant scene measurement to compute the calibrated antenna temperature.

Antenna temperature at internal calibration plane

The antenna temperature at the internal calibration plane is computed from

$$\overline{T}_A'' = \left(\overline{\overline{G}}^T \overline{\overline{G}}\right)^{-1} \overline{\overline{G}}^T \left(\overline{C}_{AA} - \overline{o}\right) \tag{3.25}$$

where the low-pass filtered gain matrix (G) and low-pass filtered offset vector (o) have been interpolated to the time of the antenna counts measurement.

Antenna temperature at feed horn

The antenna temperature computed in 3.25 must be propagated through the front end, accounting for the signal loss and phase difference from the front-end. The antenna temperature referenced to the feed horn is computed by inverting the forward radiative transfer equation through the front end, accounting for the losses and polarimetric mixing. This is represented as,

$$\begin{aligned} \overline{T}_A &= A^{-1}\left[\overline{T}_A'' - \left(\overline{\overline{I}} - \overline{\overline{\Gamma}}_{A-R}\right)\left(\overline{\overline{I}} - \overline{\overline{L}}_2\right)\overline{\overline{L}}_{FEM}\overline{T}_{FEM} - \left(\overline{\overline{I}} - \overline{\overline{\Gamma}}_{A-R}\right)\overline{\overline{L}}_2\overline{T}_2 - \overline{\overline{\Gamma}}_{A-R}\overline{T}_{iso}\right] \\ A &= \left(\overline{\overline{I}} - \overline{\overline{\Gamma}}_{A-R}\right)\left(\overline{\overline{I}} - \overline{\overline{L}}_2\right)\left(\overline{\overline{I}} - \overline{\overline{L}}_{FEM}\right)M_{FEM} \end{aligned} \tag{3.26}$$

where the Mueller matrix for the front end manifold reduces to just the phase imbalance since the amplitude imbalance is handled through the loss terms,

$$M_{FEM} = \begin{bmatrix} 1 & 0 & 0 & 0 \\ 0 & 1 & 0 & 0 \\ 0 & 0 & \cos\left(\Delta\theta_{FEM}\right) & \sin\left(\Delta\theta_{FEM}\right) \\ 0 & 0 & -\sin\left(\Delta\theta_{FEM}\right) & \cos\left(\Delta\theta_{FEM}\right) \end{bmatrix}. \tag{3.26b}$$

The differential phase difference through the front-end V/H-pol paths is parameterized as a linear combination of the temperature difference between the front-end components

$$\Delta\theta_{FEM} = b_{0\_\theta FEM} + \left(T_{OMTV} - T_{OMTH}\right)b_{1\_\theta FEM} + \left(T_{WGV} - T_{WGH}\right)b_{2\_\theta FEM} + \left(T_{CPLRV} - T_{CPLRH}\right)b_{3\_\theta FEM}. \tag{3.26c}$$

and the front-end loss is accounted for by,

$$L_{FEM} = \begin{bmatrix} L_{V,FEM} & 0 & 0 & 0 \\ 0 & L_{H,FEM} & 0 & 0 \\ 0 & 0 & \sqrt{L_{V,FEM}L_{H,FEM}} & 0 \\ 0 & 0 & 0 & \sqrt{L_{V,FEM}L_{H,FEM}} \end{bmatrix} \tag{3.26d}$$

The loss and reflections at the second plane are given by,

$$L_2 = \begin{bmatrix} L_{V,2} & 0 & 0 & 0 \\ 0 & L_{H,2} & 0 & 0 \\ 0 & 0 & \sqrt{L_{V,2}L_{H,2}} & 0 \\ 0 & 0 & 0 & \sqrt{L_{V,2}L_{H,2}} \end{bmatrix} \tag{3.26e}$$

$$\Gamma_{A\_R} = \begin{bmatrix} \Gamma_V & 0 & 0 & 0 \\ 0 & \Gamma_H & 0 & 0 \\ 0 & 0 & \sqrt{\Gamma_V\Gamma_H} & 0 \\ 0 & 0 & 0 & \sqrt{\Gamma_V\Gamma_H} \end{bmatrix} \tag{3.26f}$$

The thermal contribution from the front end is given by the vector,

$$\overline{T}_{FEM} = \begin{bmatrix} T_{FEM\_V} \\ T_{FEM\_H} \\ 0 \\ 0 \end{bmatrix} \tag{3.26g}$$

And the thermal contribution that is reflected at the assumed internal reflection plane is given by the internal receiver physical temperature at the isolator,

$$\overline{T}_{iso} = \begin{bmatrix} T_{RV} \\ T_{RH} \\ 0 \\ 0 \end{bmatrix} \tag{3.26h}$$

In the above equations, the physical temperatures used in the equations come from the thermistor measurements that are linearly interpolated to the time of the scene measurement. The loss, reflection and phase imbalance parameters are derived during pre-launch calibration and tuned post-launch. Values for these coefficients are contained in the COWVR pre-launch calibration report. The latest values can always be found in the COWVR ground system parameter files.

4.3. Brightness Temperature Calibration

The antenna temperature referenced to the feed in equation 3.26 consists of contributions from the Earth and the cold sky background weighed by the antenna pattern. These contributions must be removed using the pre-launch antenna patterns.

4.3.1. Spill-over Correction

The first correction is to remove the cold sky contribution and rescale the antenna temperature to be the power received from within the Earth horizon. The COWVR antenna patterns vary subtlety with azimuth position. Therefore, the antenna pattern correction parameters are allowed to vary

with azimuth position Φ. The cold sky correction is represented as,

$$T_{B,p}^{Earth}(\Phi) = \eta_{Earth,p}^{-1}(\Phi)\left[T_{A,p}(\Phi) - \left(1-\eta_{Earth,p}(\Phi)\right)T_{sky,p}\right]$$
$$p = V,H \tag{3.27a}$$

and

$$T_{B,p}^{Earth}(\Phi) = \eta_{Earth,p}^{-1}(\Phi)\left[T_{A,p}(\Phi)\right]$$
$$p = 3,4 \tag{3.27b}$$

where $\eta_{Earth,p}$ is the fraction of power received by the antenna that is beyond the Earth horizon and $T_{sky,p}$ is the cold sky background temperature of approximately 2.7 K. For COWVR, this value is about 2.3% at 18.7, 1.7% at 23.8 and 0.7% at 33.9 GHz. Note, the polarization of the sky background is small enough to be ignored for COWVR, hence the 3rd and 4th stokes channels only need to be scaled by the spill-over fraction.

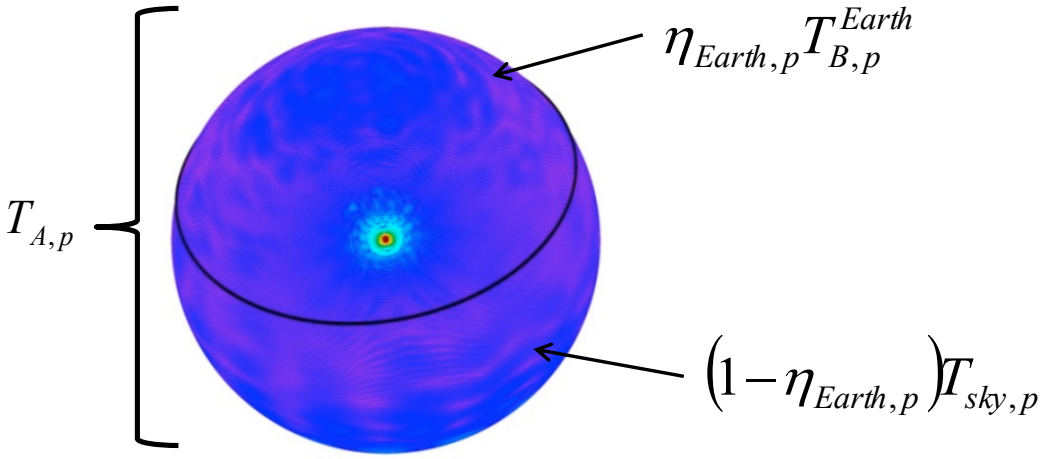

Figure 3.3-1. Image of the COWVR antenna pattern in the spacecraft coordinate frame. The black line represents the Earth horizon beyond which is only emission from cold space.

4.3.2. Cross-pol Correction

The antenna also mixes the received polarization between the polarizations. The next step is to unmix the power between the ports. This is done using a cross-pol correction matrix

$$\begin{bmatrix} T_{MBI,V}(\Phi) \\ T_{MBI,H}(\Phi) \\ T_{MBI,3}(\Phi) \\ T_{MBI,4}(\Phi) \end{bmatrix} = \begin{bmatrix} a_{VV} & a_{VH} & a_{V3} & a_{V4} \\ a_{HV} & a_{HH} & a_{H3} & a_{H4} \\ a_{3V} & a_{3H} & a_{33} & a_{34} \\ a_{4V} & a_{4H} & a_{43} & a_{44} \end{bmatrix}_{\Phi}^{-1} \begin{bmatrix} T_{Earth,V}(\Phi) \\ T_{Earth,H}(\Phi) \\ T_{Earth,3}(\Phi) \\ T_{Earth,4}(\Phi) \end{bmatrix} \tag{3.28}$$

where the *a* terms are integrated co-pol and cross-pol coupling coefficients determined from integrating the antenna patterns. An example of the antenna pattern matrix and the matrix determined from integration is shown in Figure 3.3-2 for the 18.7 GHz patterns.

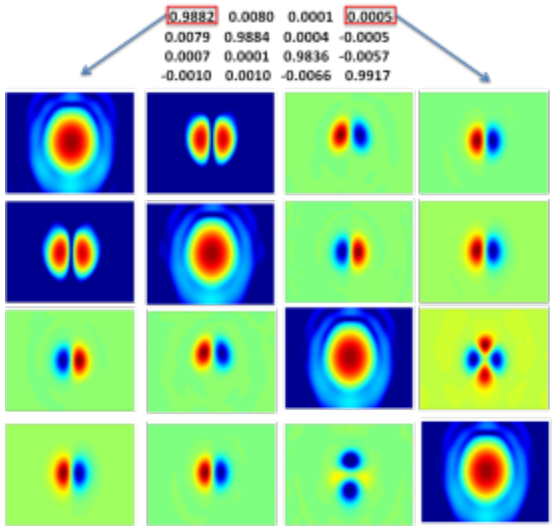

Figure 3.3-2. COWVR main beam cross-pol matrix.

It can be seen from Figure 3.3-2 that the off-diagonal cross-pol terms for the 3rd and 4th stokes channels are sensitive to the spatial derivative of the brightness temperature because the lobes have positive and negative values owing to phase variation across the mainbeam. The heritage cross-pol correction algorithm in eqn 3.28 was derived for non-polarimetric sensors and assumes a homogenous scene. For scenes with strong spatial gradients of brightness temperature (such as rain cells and coastlines), an expanded correction can be considered. The approach is use to the multiple co-pol samples to determine a more accurate cross-pol contamination correction in areas with strong brightness temperature gradients. This correction has the form,

$$T_{MB,V} = \frac{1}{a_{VV}} \left(T_{A,V} - \sum_{i,j} c_{VH}(i,j) T_{A,H}(i,j) - \sum_{i,j} c_{V3}(i,j) T_{A,3}(i,j) - \sum_{i,j} c_{V4}(i,j) T_{A,4}(i,j) \right) \tag{3.29}$$

where

$$\begin{aligned} a_{V\beta} &= \sum_{i,j} c_{V\beta}(i,j) \\ \beta &= H,3,4 \end{aligned} \tag{3.30}$$

Eq 3.29 is equivalent to 3.28 when only the i,j pairs equal to 0 are used. An illustration of the COWVR sampling relative to cross-pol lobes is shown in Figure 3.3-3. It can be seen that most of the variability can be corrected with just one or two additional samples in the cross-track and along-track directions.

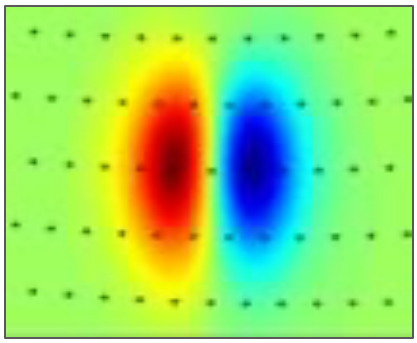

Figure 3.3-3. Illustration of the sampling pattern with respect to the cross-pol lobes for one measurement.

This algorithm was tested using randomly selected scenes from the WindSat 37 GHz channel which provides a representative brightness temperature field in terms of the spatial structures that COWVR will encounter over the ocean. The WindSat TB data were convolved with the COWVR antenna patterns to generate synthetic fully polarimetric antenna temperatures. These were then corrected for cross-pol using either eqn 3.28 or 3.29. The results are shown in Figure 3.3-4. The RMS error for both is < 0.1K, but the multi-sample algorithm eliminates errors near precipitation cells that can be as high as 0.5K. The error estimated for eqn 3.29 is < 0.05K.

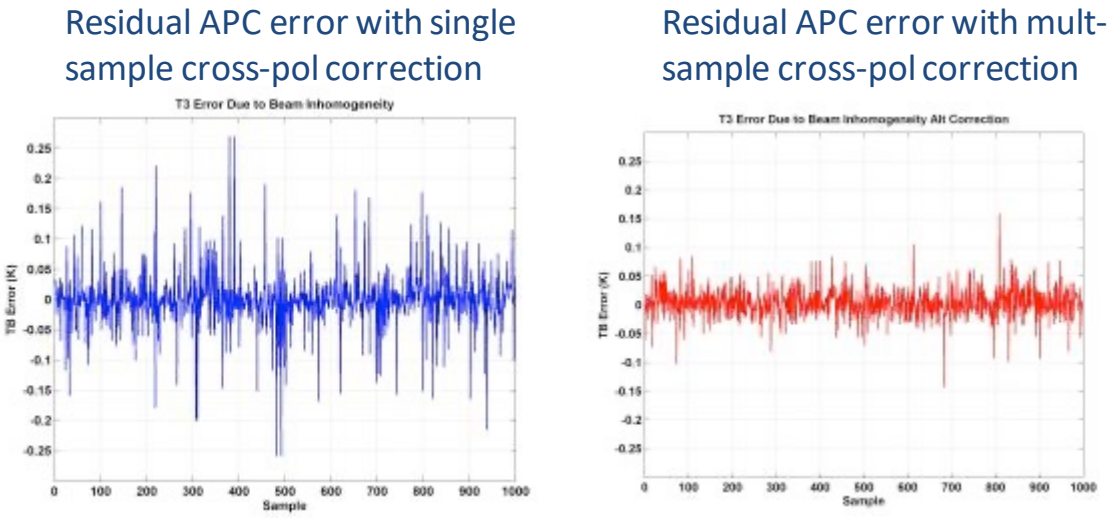

Figure 3.3-4. Residual error from the cross-pol correction using Eqn 3.28 (left) and 3.29 (right) tested on WindSat 37 GHz data. The largest errors on the left plot are from precipitation cells.

4.3.3. Polarization Basis Rotation Correction

The final correction accounts for the geometric rotation between the fixed COWVR polarization basis and Earth polarization basis.

$$\begin{bmatrix} T_{MB,V}(\Phi) \\ T_{MB,H}(\Phi) \\ T_{MB,3}(\Phi) \\ T_{MB,4}(\Phi) \end{bmatrix} = \begin{bmatrix} \cos^2(\alpha) & \sin^2(\alpha) & -\frac{1}{2}\sin(2\alpha) & 0 \\ \sin^2(\alpha) & \cos^2(\alpha) & \frac{1}{2}\sin(2\alpha) & 0 \\ \sin(2\alpha) & -\sin(2\alpha) & \cos(2\alpha) & 0 \\ 0 & 0 & 0 & 1 \end{bmatrix} \begin{bmatrix} T_{MBI,V}(\Phi) \\ T_{MBI,H}(\Phi) \\ T_{MBI,3}(\Phi) \\ T_{MBI,4}(\Phi) \end{bmatrix} \tag{3.31}$$

where the polarization rotation angle is determined by the instrument geometry and satellite attitude and corresponds to the angle at the center of the integration period. The main beam brightness in equation 3.31 is the IFOV brightness temperature for each frequency in the Earth polarization basis.

4.3.4. Resampling to the Composite Field of View (CFOV)

A re-sampling algorithm is then applied to obtain the brightness temperatures (T_B) at a 40 km cumulative field-of-view (CFOV). The CFOV is defined as a circular Gaussian pattern with a 3-dB contour at 40km, as illustrated in Figure 3.3-5.

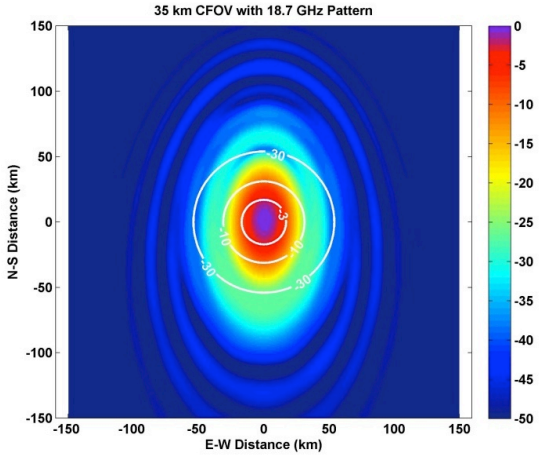

Figure 3.3-5. Illustration of the COWVR main beam pattern and the CFOV contours.

The COWVR IFOV data can be re-sampled to the CFOV using a NxM 2-D weighted average of neighboring samples for each measurement. This is represented by,

$$T_{B,p}^{CFOV}(i_0, j_0) = \sum_i \sum_j w_{i,j} T_{MB,p}(i, j) \tag{3.32}$$

where the coefficients are determined using the Backus-Gilbert technique. This technique seeks to find the set of weighting coefficients that best produce the desired sampling pattern using the instrument IFOV antenna pattern and sampling characteristics, as illustrated in Figure 3.3-6. As illustrated Figure 3.3-7, the sampling pattern on the ground varies with scan position, so the weighting coefficients must be a function of scan position.

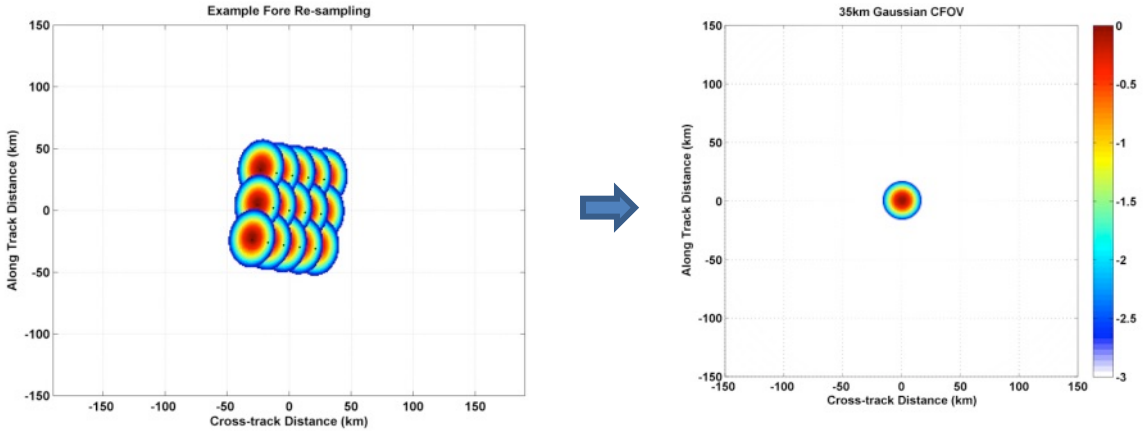

Figure 3.3-6. Illustration of a the resampling process for a 3x5 weighting matrix.

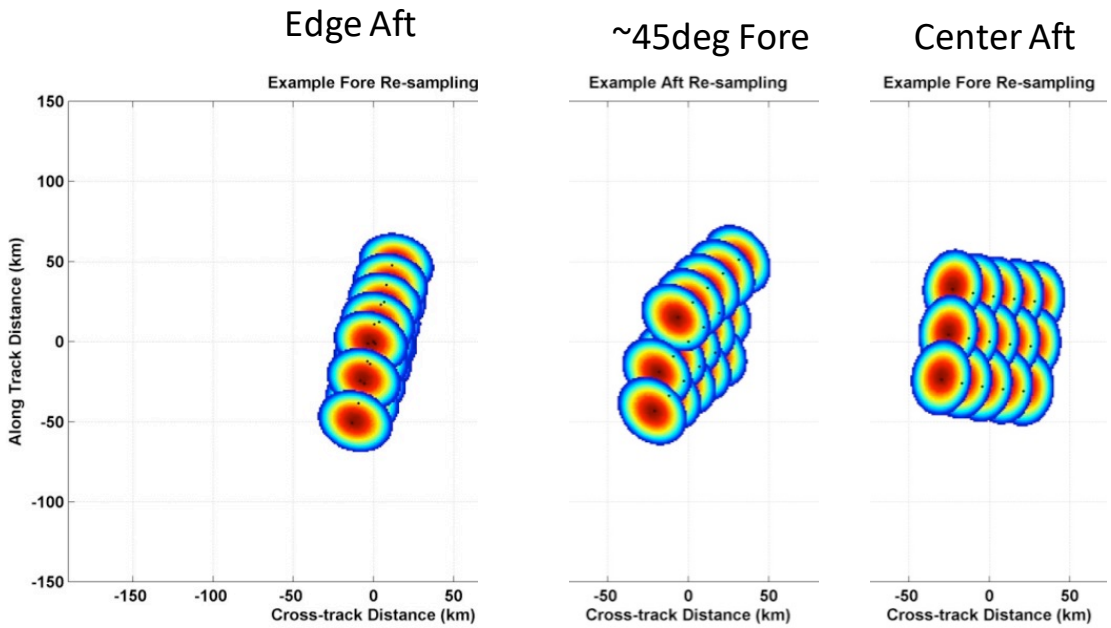

Figure 3.3-7. Sampling pattern at the center, middle and edge of scan.

To implement the resampling as a function of scan position, the COWVR data are first organized into 2-D image matrices for the fore and aft scans where each cross-track index corresponds to a scan angle relative to the spacecraft velocity vector. Because the COWVR scan rate is not fixed, the number of samples per scan can vary, so the image matrix is padded with extra elements at

the edges, where the center of the scan (closet angle to the S/C velocity vector) is placed in the center position of the matrix. This is illustrated in Figure 3.3-8. With this implementation, the weighting coefficients will only vary with row position across the scan (y-axis in Figure 3.3-8). The brightness temperature from eqn 3.32 (illustrated in the second panel of 3.3-8) is the final calibrated TB product that is provided to the EDR processor. This brightness temperature has an equal spatial sampling function at all frequencies and all directions away from the boresight for both the fore and aft data.

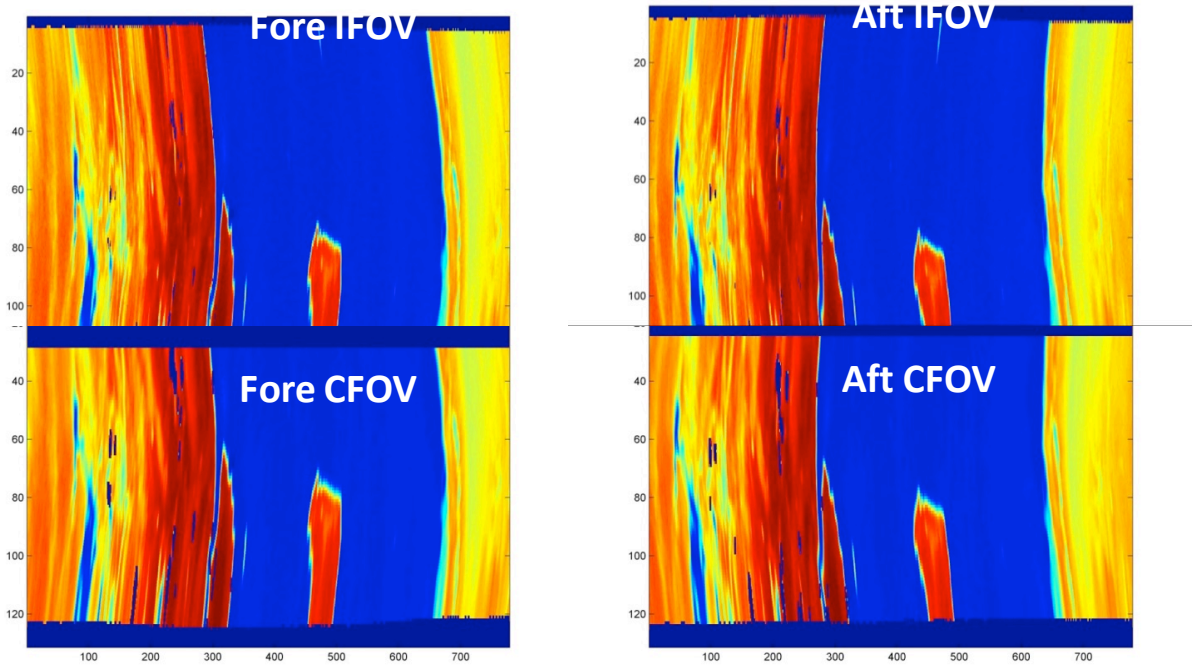

Figure 3.3-8. Illustration of COWVR data matrix for fore and aft scans during resampling.

5.0 COWVR Geophysical Retrieval Algorithm

The wind vector retrieval algorithm closely follows the algorithm developed for WindSat described in Brown et al., 2006. The atmospheric retrievals and flags are computed using the average of the fore and aft data. The wind vector retrieval algorithm uses the fore/aft data separately as described below.

5.1. Fore/Aft Image Combining and Gridding

The first step toward retrieving geophysical quantities is to resample the fore/aft CFOV image data to a common Earth referenced grid. The fore/aft data for all frequencies have been re-sampled to have an equal spatial response at the surface in all directions. Therefore, a gridding or interpolation method can be applied to resample the data from the irregular scan grid to a regular Earth fixed grid. The baseline approach is to interpolate the aft swath data to the sample locations in the forward swath using bi-cubic interpolation. An example of the fore and aft swath sampling pattern on a representative image is shown in Figure 5-1.

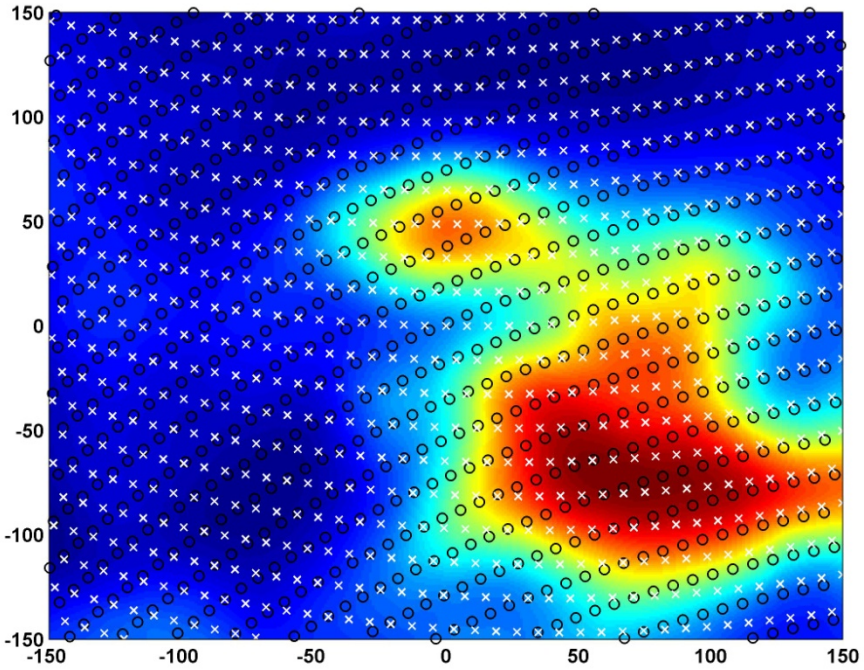

Figure 5-1. Illustration of the fore samples (black dots) and after samples (white x's) over laid on a background TB image from WindSat.

Along with gridding the data, an estimate of the inhomegeneity of the scene (mainly from the atmosphere) must be computed. This is computed by taking the spatial sample standard deviation of the fore/aft differences from neighboring samples near each grid point. This standard deviation should approach sqrt(2) times the NEDT at the CFOV. Higher standard deviations represent inhomegeneity in the scene for the different look directions. This standard deviation is applied as an inverse weight in the wind direction retrieval algorithm for the V- and H-pol fore/aft differences (discussed later).

This method was applied to WindSat data for illustration. Figure 5-2 shows a map of the spatial standard deviation in the 37 GHz channel and Figure 5-3 shows a PDF and CDF of the data. It can be seen that the higher standard deviations are associated with clouds/precipitation, but most of the points are close to the lower theoretical NEDT limit.

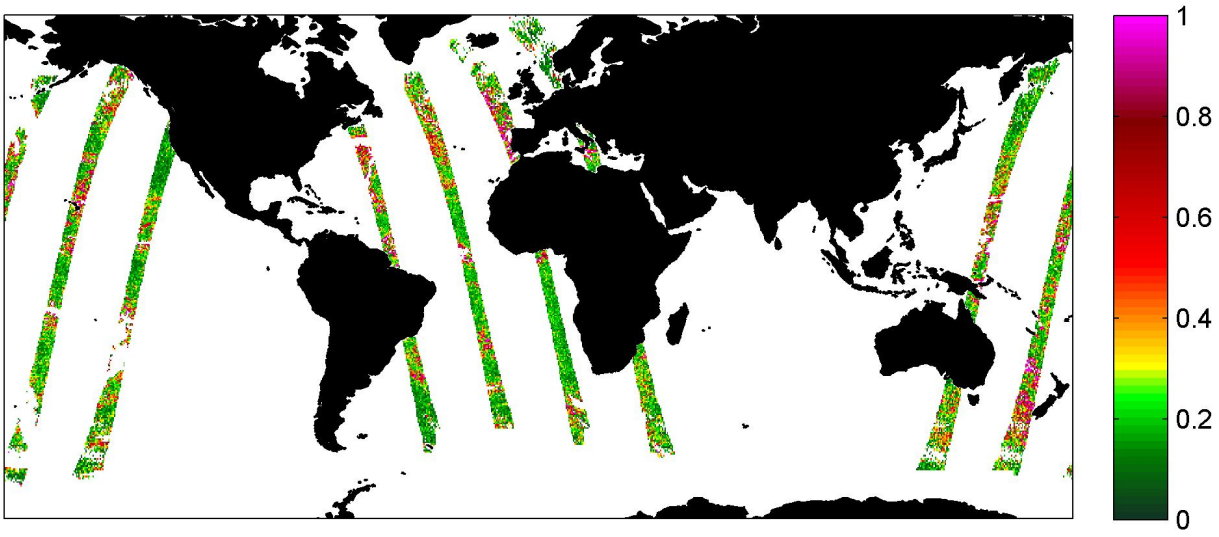

Figure 5-3. Spatial standard deviation of the fore/aft differences in the WindSat 37 GHz channel.

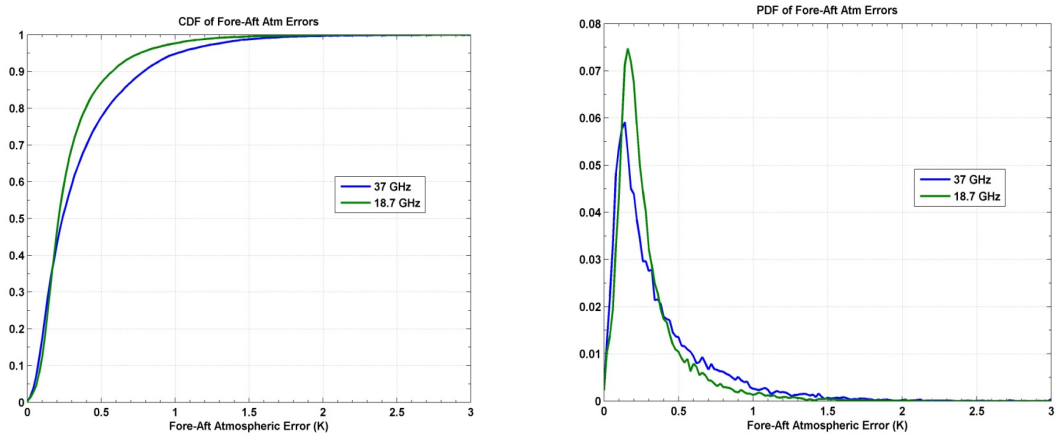

Figure 5-3. CDF (left) and PDF (right) of the spatial standard deviation of WindSat data at 18.7 and 37 GHz.

5.2. Atmospheric Parameter Estimation

The ocean surface wind vector can be estimated from the brightness temperatures provided that they are referenced to the surface, accounting for the atmospheric contribution in between the sensor and the surface. The atmospheric parameters are retrieved using a single layer, non-scattering parameterized radiative transfer equation. The main quantities that are estimated are

integrated water vapor and cloud liquid water for non-raining conditions.

The top-of-atmosphere brightness temperature can be represented,

$$T_B(f,p,\theta) = \varepsilon(f,p,\theta)T_{surf}e^{-\tau(f)\sec\theta} + T_{UP}(f,\theta) + \Gamma\left(T_{DOWN}(f,\theta) + T_{\cos mic}e^{-\tau(f)\sec\theta}\right)e^{-\tau(f)\sec\theta} \quad (5.1a)$$

where

T_B	*measured brightness temperature,*
θ	*incidence angle,*
f	*frequency,*
p	*polarization,*
T_{surf}	*sea surface temperature (K),*
ε	*surface emissivity,*
T_{UP}	*atmospheric upwelling brightness temperature,*
T_{DOWN}	*atmospheric downwelling brightness temperature,*
T_{cosmic}	*cosmic background brightness temperature,*
$\tau(f)$	*zenith integrated atmospheric optical depth as a function of frequency*
Γ	*surface reflectivity*.

which simplifies to the following for the 3rd and 4th stokes channels,

$$T_{B\_pol}(f,p,\theta) = \varepsilon(f,p,\theta)\left(T_{surf}e^{-\tau(f)\sec\theta} - \Gamma\left(T_{DOWN}(f,\theta) + T_{\cos mic}e^{-\tau(f)\sec\theta}\right)\right) \quad (5.1b)$$

For a specular ocean surface, the power reflectivity, Γ, can be expressed as 1 – ε. This specular condition is only strictly valid for a perfectly flat ocean surface, although it is assumed in many radiometric retrieval algorithms for wind roughened ocean surfaces. The reflected downwelling brightness for a slightly roughened ocean surface will largely originate from the specular direction, but as the surface roughness increases (i.e. wind speed increases) a larger amount of reflected energy will originate at angles of incidence that are larger and smaller than the specular direction. The net effect of this will cause the true reflected downwelling brightness to increase from the specular value since the atmospheric brightness scales with the secant of the incidence angle. This is accounted for using a scaling factor, **Ω**, representing the ratio of the "true" reflectivity to the specular reflectivity,

$$\Gamma = \Omega(1-\varepsilon). \quad (5.2)$$

Ω is allowed to vary with wind speed only and is taken to be the average value over all wind directions for a given wind speed. Neglecting the directional and atmospheric dependence of **Ω** is not expected to have a large impact on the retrieval since the correction factor itself is small.

5.2.1. Atmospheric Path Attenuation

The optical depth of a non-raining atmosphere for a given frequency can be expressed with high accuracy as a polynomial function of the integrated water vapor (V) in cm and cloud liquid water (L) in mm

$$\tau(f) = c_{0,f} + c_{1,f}V + c_{2,f}V^2 + c_{3,f}L + c_{4.f}L^2 \ , \tag{5.3}$$

where the frequency dependent coefficients are determined by a regression analysis (described below).

5.2.2. Upwelling and Downwelling Atmospheric TB

For a single layer, non-scattering atmosphere, the upwelling and downwelling atmospheric brightness temperatures can be approximated as a function of the optical depth

$$T_{UP}(f,\theta) = \left(1 - e^{-\tau(f)\sec\theta}\right) T_{eff}^{UP}(f), \tag{5.4a}$$

$$T_{DOWN}(f,\theta) = \left(1 - e^{-\tau(f)\sec\theta}\right) T_{eff}^{DOWN}(f), \tag{5.4b}$$

where T_{eff}^{UP} and T_{eff}^{DOWN} are atmospheric effective radiating temperatures that are as a function of frequency and location. The effective radiating temperatures for each retrieval are interpolated from look-up tables computed from NAVGEM atmospheric profile inputs. This atmospheric model for T_{UP} and T_{DOWN} has been shown to be a good approximation to the complete integral solution [3], which would require knowledge of the actual atmospheric profile of temperature, pressure, water vapor and cloud liquid water.

5.2.3. Surface Emissivity

The surface emissivity is expressed as specular component and rough surface component that is primarily due to wind.

$$\varepsilon_{surface} = \varepsilon_{specular}(f, SST, SSS, \theta, p) + \varepsilon_{wind}(f, SST, \theta, p, WS, WDIR). \tag{5.5}$$

The specular component is estimated from the Klein-Swift sea water dielectric model (Klein and Swift, 1976) using ancillary sea surface temperature and salinity data. The excess emissivity is parameterized primarily as a function of wind speed and direction, but allows for a dependence with sea surface temperature and incidence angle. Both are a function of frequency and polarization.

5.2.4. Wind Emissivity Geophysical Model Function

The emissivity of the ocean surface for the V/H-pol channels be expressed as an even Fourier series and the 3rd/4th stokes channels can be expressed as an odd Fourier series [4-6]. For a given

frequency, this is represented to the second harmonic as,

$$\varepsilon_{V,H}\left(WS,\varphi,SST\right)=a_{0,p}\left(WS,SST,\theta\right)+a_{1,p}(WS)\cos\varphi+a_{2,p}(WS)\cos 2\varphi, \tag{5.6a}$$

$$\varepsilon_{3,4}\left(WS,\phi\right)=b_{0,p}+b_{1,p}(WS)\sin\phi+b_{2,p}(WS)\sin 2\phi\ , \tag{5.6b}$$

where $\phi=\phi_R-\phi_W$ is the angle between the look direction of the radiometer, ϕ_R, and the direction the wind is blowing from, ϕ_W. ϕ_W is referenced to the compass with 0° as North and 90° as East. A relative direction of 0° is generally referred to as the upwind direction, *i.e.* with the wind blowing toward the radiometer. The coefficients in Eqn. (4.8) are functions of wind speed, sea surface temperature, incidence angle, frequency and polarization. The first and second order harmonic coefficients ($a_{1,2}$,$b_{1,2}$) have a first order dependence on the surface wind speed. The dependence of these coefficients on other environmental parameters such as the salinity and air-sea temperature difference is generally much weaker. They are, therefore, assumed to vary only with wind speed for a given channel. The zeroth order harmonics for v- and h-pol increase generally monotonically with wind speed and reduce to zero wind speed approaches zero. The coefficients in 4.8 are best determined empirically from the data, as physical models still fall short of accurately characterizing the complex dependence of the emission as a function of sea state. These have been previously parameterized with WindSat and will be re-derived from COWVR data at the sensors specific center frequencies and incidence angle. The functional form empirical isotropic rough emissivity function is adopted from Meissner and Wentz (2012) which includes a fifth order polynominal function of wind speed and small linear corrections for the variation with incidence angle and sea surface temperature. The b_0 coefficient is nominally zero, but is retained for account for any calibration offsets.

Because COWVR has a complete fore and aft scan, synthetic channels can be created from the fore minus aft difference for the V-pol and H-pol channels. At the surface, this difference is a function of the wind direction and is represented by,

$$\begin{aligned}\varepsilon_{V\_fore}-\varepsilon_{V\_aft}=&-2a_1\sin\left(\frac{\varphi_{caa\_fore}+\varphi_{caa\_aft}}{2}-\varphi_{wind}\right)\sin\left(\frac{\varphi_{caa\_fore}-\varphi_{caa\_aft}}{2}\right)-\\&2a_2\sin\left(\varphi_{caa\_fore}+\varphi_{caa\_aft}-2\varphi_{wind}\right)\sin\left(\varphi_{caa\_fore}-\varphi_{caa\_aft}\right)\end{aligned} \tag{5.7}$$

where φ represents the compass angles of either the forward or aft look directions or wind speed. The first sine term describes the wind direction dependence and the second sine term describes the dependence with look direction angle difference (which in the case of COWVR is along the scan arc). The benefit of using the V-pol and H-pol fore-aft difference is that the strong isotropic wind speed signal is removed and the atmospheric contribution is greatly reduced.

Figure 5-4 shows example model functions derived from WindSat data at 1m/s and 7m/s. At low wind speeds, the signal in the 3rd/4th stokes channels is negligible, while there is some usable signal in the V-pol fore-aft difference.

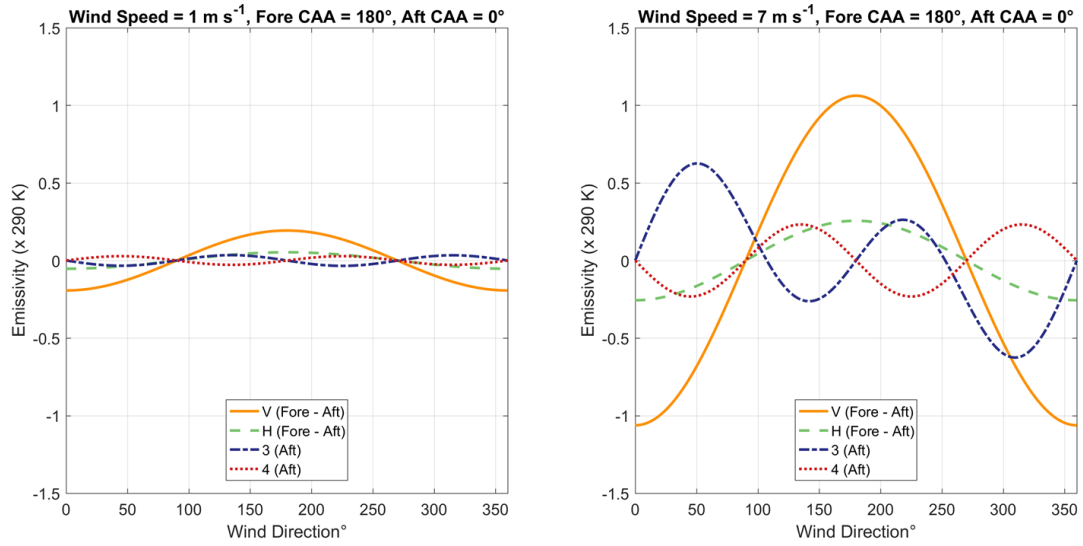

Figure 5-4. Dependence of the V/H-pol fore-aft and 3rd/4th stokes brightness with relative wind direction at 1m/s and 7m/s.

5.3. Retrieval Methodology

Section 5.2 describes the forward model relating the geophysical parameters to be retrieved to the top of atmosphere brightness temperatures. Given a set of COWVR measurements, the atmospheric and surface properties are estimated. First, the precipitable water vapor, integrated cloud liquid and wind speed are estimated using an iterative Newton-Raphson method with the V-pol and H-pol channels only. In this first step, an ancillary wind direction is used. Once *V*, *L* and *WS* are estimated, the surface emissivity is estimated by inverting eqns 5.1. The specular component is subtracted from the V-pol and H-pol emissivity leaving the component due to wind.

Given a set of measured emissivies derived from the COWVR top-of-atmosphere TB data, a maximum likelihood estimator is used to solve for wind vector. This is done by minimizing the cost function,

$$\Phi(WS,\phi) = SST * \left\{ \sum_{f} \sum_{p} \left(w_{f,p} \left[\varepsilon_{f,p} - GMF(f,p,WS,\phi) \right] \right)^2 \right\}^{1/2}, \qquad (5.8)$$

where *f* is frequency, *p* is polarization and $w_{f,p}$ are normalized weights for each channel and the equation is scaled by the surface temperature (*SST*). The solution is performed in two steps. In the first step, the prior solution for wind speed is used and the wind direction solutions (up to 4) are found and ranked using the V/H-pol fore-aft difference, 3rd and 4th stokes channels. The channel weights are a combination of the individual channel noise and the so-called model noise. The channel noise is determined from the pre-launch instrument characterization and is fixed. The model noise primarily arises from the atmospheric uncertainty that is computed as described above. The first step direction solutions are then used in a second step to refine the wind speed

estimate using the V-pol and H-pol channels without taking the fore-aft difference.

6.0 References

[1] Piepmeier, J.R.; Long, D.G.; Njoku, E.G., "Stokes Antenna Temperatures," *Geoscience and Remote Sensing, IEEE Transactions on* , vol.46, no.2, pp.516,527, Feb. 2008
doi: 10.1109/TGRS.2007.909597

[2] Piepmeier, J.R.; Kim, E. J., "Calibration of passive microwave hybrid coupler-based polarimeters," *Geoscience and Remote Sensing Symposium, 2003. IGARSS '03. Proceedings. 2003 IEEE International* , vol.2, no., pp.1244,1246 vol.2, 21-25 July 2003
doi: 10.1109/IGARSS.2003.1294071

[3] Wentz F., "A well-calibrated ocean algorithm for special sensor microwave / imager," J. Geophys. Res. 102(C4), pp 8703-8718, 1997.

[4] Yueh, S., W. Wilson, F. Nghiem and W. Ricketts, "Polarimetric Measurements of Sea Surface Brightness Temperatures Using an Aircraft K-band Radiometer," IEEE Trans. Geosci. Rem. Sens. 33(1) pp. 85-92. Jan, 1995.

[5] Yueh, S., W. Wilson, S. Dinardo and F. Li, "Polarimetric Microwave Brightness Signatures of Ocean Wind Directions," IEEE. Trans. Geosci. Rem. Sens., 37(2), pp 949-959, 1999.

[6] Yueh, S. R. Kwok, F. Li, S. Nghiem, W. Wilson and J. Kong, "Polarimetric Passive Remote Sensing of Random Discrete Scatterers and Rough Surfaces," Radio Sci., pp 799-814, 1994.

[7] Klein L. A. and C. T. Swift, "An improved model for the dielectric constant of sea water at microwave frequencies," IEEE Trans. Ant. Propogat, 25, pp 104-111, 1976.

[8] Brown, S. T., Ruf, C. S., & Lyzenga, D. R. (2006). An emissivity-based wind vector retrieval algorithm for the WindSat polarimetric radiometer. *IEEE transactions on geoscience and remote sensing*, *44*(3), 611-621.

[9] Meissner, T., & Wentz, F. J. (2012). The emissivity of the ocean surface between 6 and 90 GHz over a large range of wind speeds and earth incidence angles. *IEEE Transactions on Geoscience and Remote Sensing*, *50*(8), 3004-3026.